Available online at www.sciencedirect.com
SCIENCE DIRECT®
Journal of Computational Physics 205 (2005) 567–610
JOURNAL OF COMPUTATIONAL PHYSICS
www.elsevier.com/locate/jcp

Modelling evaporation fronts with reactive Riemann solvers

O. Le Métayer [a,b], J. Massoni [a,b], R. Saurel [a,b,c,*]

[a] *IUSTI, UMR CNRS 6595, Université Aix-Marseille I, Technopôle de Château Gombert, 5 Rue E. Fermi, 13453 Marseille Cedex 13, France*
[b] *Projet SMASH, INRIA, 2004 route des Lucioles, 06902 Sophia Antipolis, France*
[c] *Institut Universitaire de France, Technopôle de Château Gombert, 5 Rue E. Fermi, 13453 Marseille Cedex 13, France*

Received 16 July 2004; received in revised form 19 November 2004; accepted 22 November 2004
Available online 30 December 2004

Abstract

This work deals with the modelling of permeable fronts and the building of a numerical method allowing the multi-dimensional propagation of such fronts. A particular attention is given to evaporation waves that appear in cavitating systems. These ones are considered as discontinuities through which a non-equilibrium liquid turns to a liquid–vapor mixture at thermodynamic equilibrium. Such transformation occurs at finite rate. In order to determine this kinetics, the evaporation front is assumed to propagate at the maximum admissible speed corresponding to the Chapman–Jouguet deflagration point [J.R., Simões-Moreira, J.E., Shepherd, Evaporation waves in superheated dodecane, J. Fluid Mech. 382 (1999) 63–86]. Using this particular kinetic relation, Rankine–Hugoniot relations are closed at such fronts. Then it is possible to solve the associated reactive Riemann problem. However, another difficulty is present to solve the multi-dimensional propagation of permeable fronts. This kind of front is subsonic and a conventional averaging scheme (such as Godunov scheme) is inappropriate. To overcome this difficulty, the reactive Riemann problem solution is embedded into the discrete equations method (DEM) [R., Abgrall, R., Saurel, Discrete equations for physical and numerical compressible multiphase mixtures, J. Comp. Phys. 186 (2003) 361–396; R., Saurel, S., Gavrilyuk, F., Renaud, A multiphase model with internal degrees of freedom: application to Shock–Bubble Interaction, J. Fluid. Mech., 495 (2003) 283–321]. This numerical method necessitates deep extensions that are detailed herein. Numerical results are shown and validated over experimental data. Some examples show that the same method may be applied to the propagation of detonation fronts.

Keywords: Evaporation; Cavitation; Detonation; Kinetic relation; CJ deflagration; Reactive Riemann solver; Subsonic fronts; Discrete equation method; Hyperbolic

* Corresponding author.
E-mail addresses: olivier.lemetayer@polytech.univ-mrs.fr (O. Le Métayer), jacques.massoni@polytech.univ-mrs.fr (J. Massoni), richard.saurel@polytech.univ-mrs.fr (R. Saurel).

0021-9991/$ - see front matter © 2004 Elsevier Inc. All rights reserved.
doi:10.1016/j.jcp.2004.11.021

1. Introduction

When a liquid initially in thermodynamic equilibrium undergoes strong rarefaction waves, it may reach a metastable state where the temperature is higher than the saturated one at the final pressure of the expanded state. Then the superheated liquid releases its metastable energy (stored as internal energy) very quickly, even explosively, producing either pure vapor or liquid–vapor mixture at thermodynamic equilibrium, flowing at high velocity. This phenomenon is often called cavitation. Such situations appear frequently in nature and in many industrial applications, as liquid flows around hypervelocity projectiles, airfoils, or inside nozzles such as fuel injector systems. Cavitation in these systems always produces strong disturbances. In most applications, cavitation appears as a multi-dimensional process due to geometrical effects. This multi-dimensional character complicates both experiments and theories. By using one-dimensional expansion tubes, many authors [15,21,28,36] and particularly [32] succeeded in isolating the main phenomenon we propose to summarize hereafter. These experiments consisted in connecting a vertical tube filled with a liquid in thermodynamic equilibrium at atmospheric pressure (or higher) to a very low-pressure chamber (Fig. 1).

As soon as the membrane between the liquid and the vacuum chamber is ruptured, rarefaction waves propagate through the liquid producing a superheated liquid (Fig. 2).

Then a subsonic phase transition front propagates through the superheated liquid producing a high velocity liquid–vapor mixture in thermodynamic equilibrium towards the low-pressure chamber. The front velocity is approximately 1 m/s while the ejected mixture velocity is of the order of 100 m/s.

These experimental observations indicate that both liquid and vapor compressibilities must be considered. Another observation was provided by Reinke and Yadigaroglu [28] about the front structure. The front appears as a highly disturbed cellular discontinuity as shown in Fig. 3.

Then, if the front structure has to be computed, the appropriate model must solve the front instabilities. Typical cellular scales are of the order of 1 mm–1 μm which is very small compared to industrial systems

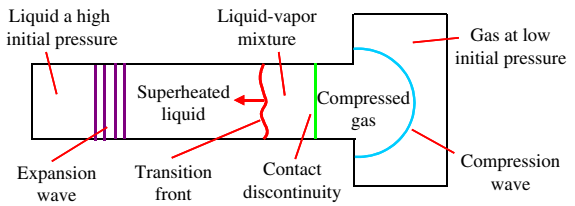

Fig. 1. Simplified experimental setup of the expansion tube in [32] and associated waves paths.

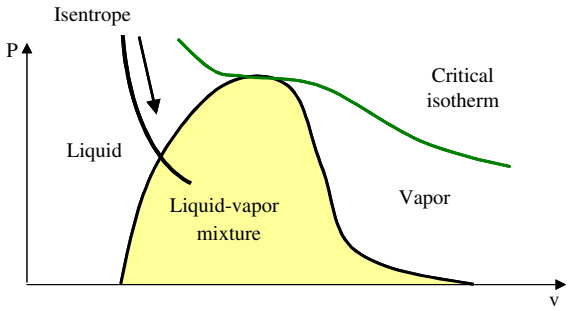

Fig. 2. Liquid thermodynamic process associated to the expansion wave producing a superheated liquid.

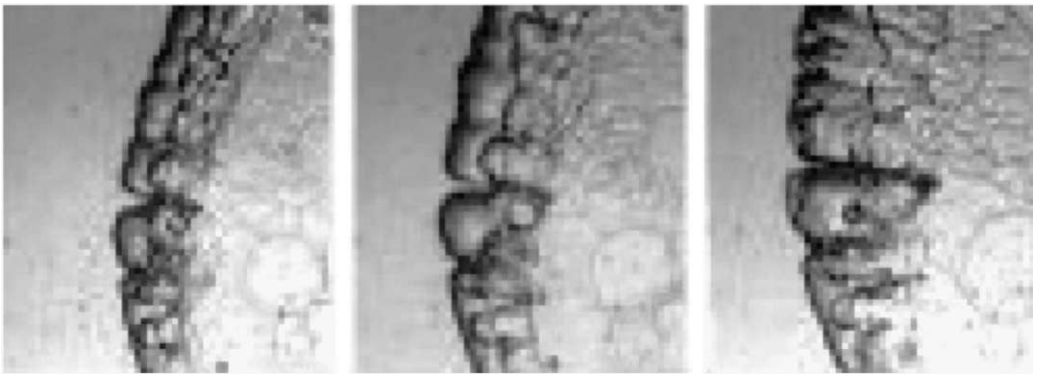

Fig. 3. Photographs from [28] showing the structure of an evaporation front.

dimensions. In addition, even if the one-dimensional structure is only considered, the heat boundary layers on both sides of the front are also very small (1 μm). In this way, several works have been achieved where the front is solved theoretically [1,22,34,38] or numerically [14,20]. For the applications under consideration (hypervelocity underwater projectiles, liquid flows in nozzles), the only reasonable approach is to consider the front as a discontinuity without solving its internal structure. This approach is adopted in the present paper. Obviously, it poses other difficulties that are summarized hereafter:

– the thermodynamic closure and associated equations of state,
– the front kinetic relation,
– the building of a reactive Riemann solver,
– the numerical treatment of the multi-dimensional front propagation.

The first difficulty deals with the thermodynamic closure. Since the front is considered as a discontinuity separating the liquid phase and a pure vapor when evaporation is total, or a liquid–vapor mixture when evaporation is partial, appropriate EOS on both sides of the front are needed to close the conservation laws. The last ones are either the Euler equations for a single phase or the homogeneous Euler equations for a liquid–vapor mixture at thermodynamic equilibrium. In the first case, pure liquid and vapor EOS are needed. In the second case, a mixture EOS must be used. Pure vapor and liquid EOS are strongly coupled. Indeed, at thermodynamic equilibrium, combination of both EOS in conjunction with pressure, temperature and chemical potential equilibrium must reproduce the phase diagram as detailed in [23]. This combination also results in a mixture EOS corresponding to the well-known saturated vapor pressure $P = P_{\mathrm{sat}}(T)$ characteristic of the liquid–vapor couple. This is the topic of Section 2.

The second and third difficulties are linked and are related to the modelling of liquid–vapor phase transition. In the experiments described below, an acoustic wave (expansion wave) is preceding the evaporation front, itself preceding a compression wave and a contact discontinuity as represented in Fig. 1. The corresponding waves pattern is shown in the (x,t) diagram in Fig. 4.

Such a configuration is known in the literature as the reactive Riemann problem. This one has been solved by [9,18,35] for detonation and deflagration problems with ideal gas EOS. For evaporation problems, it must be solved carefully. Since the front is considered as a discontinuity, the Rankine–Hugoniot relations for the Euler equations express the mass, momentum and energy conservation principles across the front. However, this front being subsonic, a precursor acoustic wave is present. In order to remove the indeterminacy produced by the extra state resulting from the precursor wave propagation, an additional relation is required: the 'kinetic relation'. This one selects the front velocity and uniqueness of the reactive

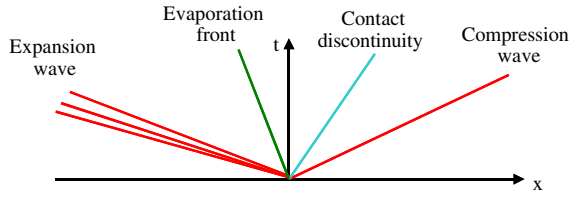

Fig. 4. A typical waves pattern of the reactive Riemann problem associated to evaporation waves.

Riemann problem solution is recovered. Among the available kinetic relations, two of them are of interest. The first one is the quasi-constant pressure deflagration, like flame fronts [10] and smooth evaporation fronts. In this case, pressure variations are very weak and temperature evolutions are inversely proportional to those of densities. Nevertheless, this is not the case for a strongly superheated liquid state where the system tends towards equilibrium as fast as possible but with a finite rate. Then the second kinetic relation, corresponding to a maximum admissible mass flow rate through the front, is of fundamental importance: the Chapman–Jouguet (CJ) deflagration point. For highly superheated liquids, the assumption of a CJ deflagration front velocity has been suggested by Simões-Moreira and Shepherd [32], as well as analogy between evaporation and deflagration fronts. In the present work, we often use the expressions 'deflagrations' and 'evaporation fronts' indifferently even if substantial differences exist between these phenomena. The reason is that the solution for both types of front belongs to the deflagration branch of the Crussard curve we shall describe in Section 3. The denomination 'deflagration branch' has an historical origin and denotes in fact the admissible locus for subsonic fronts. Thus, in [32], in the particular case of dodecane, the authors made several experiments, described in Fig. 1, involving different initial temperatures of the liquid. For each experiment, they measured the superheated liquid temperature, the pressure behind the evaporation front and the front velocity. The experimental results (symbols) are represented in Fig. 5. In the same figure, we also represent the theoretical curves (lines) corresponding to the resolution of the Rankine–Hugoniot system coupled with the CJ deflagration relation and each phase EOS.

The agreement between experimental and theoretical results being very good, this particular kinetic law is adopted in this paper. Thus this law fulfils simultaneously two important features. First, this relation allows the reactive Riemann problem closure and its resolution. Secondly, it is used in order to express the macroscopic dynamics of the front summarizing the internal mechanisms (diffusion and capillarity) as well

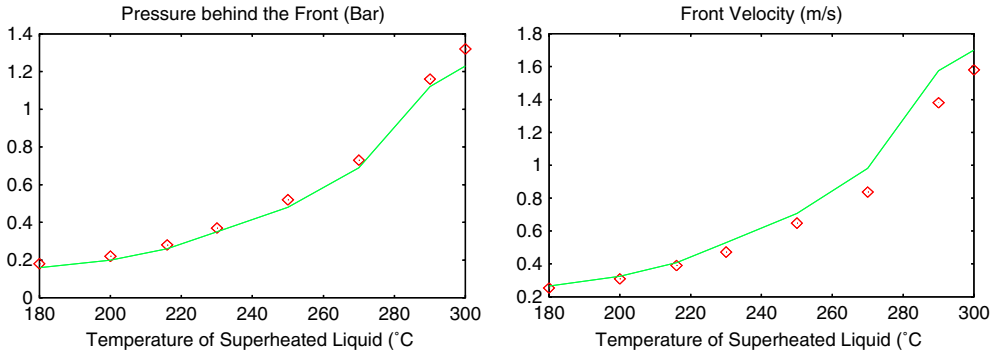

Fig. 5. Experimental (symbols) and theoretical (lines) values associated to experiments described in Fig. 1 from [32]. Theoretical values are calculated by the use of Rankine–Hugoniot relations and the CJ deflagration kinetic relation.

as multi-dimensional front instabilities. The resolution of the reactive Riemann problem associated to evaporation fronts including the CJ deflagration kinetic law is achieved in Section 3.

Nevertheless, the resolution of such a problem only provides a one-dimensional local solution. The applications mentioned before necessitate the multi-dimensional propagation of such fronts. Then, the reactive Riemann solver must be used along the front normal to determine the mass flow rate, momentum and energy transfers across the front. Nevertheless, an important remark must be expressed. Let us assume the presence of an evaporation front inside a control volume. We shall see in Section 3 that all variables (pressure, density, velocity and entropy) are strongly discontinuous through the evaporation front. In a single-phase type model, the averaging procedure inside the cell implies unique values for the different variables. Then the solutions provided by the reactive Riemann problem are irremediably lost, leading to a non-physical solution. This problem comes from the fact that fluids on both sides of the front have different thermodynamic properties. To reproduce the physical solution, we must clearly use two sub-volumes in the cell (each one corresponding to a pure fluid) and two systems of equations linked by the associated Rankine–Hugoniot relations across the front. The discrete equations method (DEM) [2,29,8] fulfils simultaneously these conditions. It consists in the integration of interface problems solutions over a two-phase control volume. Such solutions are provided by the Riemann problem. Initially developed for two-phase mixtures and interface problems, this method is extended to reactive fronts (RDEM) in Section 4. Section 5 is devoted to several validations of the method. Some illustrations showing its capabilities are also provided.

2. Determination of pure fluid equations of state

In this section, we briefly recall the method developed in [23]. Combination of the pure fluid EOS under thermodynamic equilibrium must be able to reproduce the liquid–vapor phase diagram. Thus, the various parameters of both EOS are strongly dependant. The corresponding EOS will be widely used when dealing with the reactive Riemann solver associated to evaporation fronts in Section 3.

We have chosen to represent each fluid thermodynamics by the 'Stiffened Gas' EOS [19]. Indeed, this EOS contains the main properties of the matter that are repulsive effects in gases, repulsive and attractive effects in liquids. The 'Stiffened Gas' EOS reads:

$$e(P,\rho) = \frac{P + \gamma P_\infty}{(\gamma - 1)\rho} + q, \tag{1}$$

where e, P and ρ are, respectively, the specific internal energy, the pressure and the density of the fluid. γ, P_∞ and q (energy of the fluid at a given reference state) are constant parameters, characteristic of the thermodynamic behavior of the fluid. The sound speed, for this particular EOS, reads $c^2 = (\gamma(P + P_\infty))/\rho$.

Using Maxwell laws and Gibbs identity, EOS (1) may be reformulated in function of pressure P and temperature T:

$$e(P,T) = \frac{P + \gamma P_\infty}{P + P_\infty} C_v T + q, \tag{2}$$

$$\rho(P,T) = \frac{P + P_\infty}{(\gamma - 1) C_v T}, \tag{3}$$

$$h(T) = \gamma C_v T + q, \tag{4}$$

$$s(P,T) = C_v \ln \frac{T^\gamma}{(P+P_\infty)^{\gamma-1}} + q', \tag{5}$$

$$G(P,T) = h(T) - Ts(P,T) = (\gamma C_v - q')T - C_v T \ln \frac{T^\gamma}{(P+P_\infty)^{\gamma-1}} + q, \tag{6}$$

where h, s and G are, respectively, the specific enthalpy, the specific entropy and the Gibbs function of the fluid. C_v is the heat capacity at constant volume and q' is also a characteristic constant. More details about the determination of such EOS may be found in [23].

Each pure phase is described by EOS (1) with appropriate parameters that are connected through thermodynamic equilibrium condition. Hereafter, the liquid and the vapor EOS are associated, respectively, by subscripts l and g. In order to reproduce the experimental saturation curves, we assume that both phases have the same pressure, temperature and Gibbs function. Equalling the Gibbs functions of both phases, a relation $P(T)$ is obtained, analog to the experimental saturated vapor pressure $P_{\text{sat}}(T)$:

$$\ln(P+P_{\infty,\text{g}}) = A + \frac{B}{T} + C\ln T + D\ln(P+P_{\infty,\text{l}}), \tag{7}$$

where

$$A = \frac{\gamma_\text{l} C_{v,\text{l}} - \gamma_\text{g} C_{v,\text{g}} + q'_\text{g} - q'_\text{l}}{(\gamma_\text{g}-1)C_{v,\text{g}}}, \quad B = \frac{q_\text{l} - q_\text{g}}{(\gamma_\text{g}-1)C_{v,\text{g}}}, \quad C = \frac{\gamma_\text{g} C_{v,\text{g}} - \gamma_\text{l} C_{v,\text{l}}}{(\gamma_\text{g}-1)C_{v,\text{g}}}, \quad D = \frac{(\gamma_\text{l}-1)C_{v,\text{l}}}{(\gamma_\text{g}-1)C_{v,\text{g}}}.$$

In addition, the analog to the experimental latent heat of vaporization $L_v(T)$ is obtained with the following relation:

$$L(T) = h_\text{g}(T) - h_\text{l}(T) = (\gamma_\text{g} C_{v,\text{g}} - \gamma_\text{l} C_{v,\text{l}})T + q_\text{g} - q_\text{l}. \tag{8}$$

One can show that relations (7) and (8) verify the Clausius–Clapeyron relation given by:

$$L(T) = T(v_\text{g}(T) - v_\text{l}(T))\frac{\mathrm{d}P}{\mathrm{d}T}, \tag{9}$$

where $v_\text{g} = 1/\rho_\text{g}$ and $v_\text{l} = 1/\rho_\text{l}$ are, respectively, the specific volumes of the vapor and the liquid along the saturated vapor pressure $P(T)$. Then, the fitting of the preceding theoretical saturation curves to the experimental ones, given in [26,27] for example, allows the complete determination of each phase EOS parameters. Appropriate procedures for their determination are described in [23].

For dodecane, the calculated parameters are $\gamma_\text{l} = 2.19$, $P_{\infty,\text{l}} = 4\times10^8$ Pa, $q_\text{l} = -755\times10^3$ J/kg, $q'_\text{l} = 0$ J/kg/K, $C_{v,\text{l}} = 1077$ J/kg/K, $\gamma_\text{g} = 1.025$, $P_{\infty,\text{g}} = 0$ Pa, $q_\text{g} = -237\times10^3$ J/kg, $q'_\text{g} = -24\times10^3$ J/kg/K and $C_{v,\text{g}} = 1956$ J/kg/K. For water and steam, the parameters are $\gamma_\text{l} = 2.35$, $P_{\infty,\text{l}} = 10^9$ Pa, $q_\text{l} = -1167\times10^3$ J/kg, $q'_\text{l} = 0$ J/kg/K, $C_{v,\text{l}} = 1816$ J/kg/K, $\gamma_\text{g} = 1.43$, $P_{\infty,\text{g}} = 0$ Pa, $q_\text{g} = 2030\times10^3$ J/kg, $q'_\text{g} = -23\times10^3$ J/kg/K and $C_{v,\text{g}} = 1040$ J/kg/K.

As an illustration, experimental (lines) and theoretical (dotted lines) saturation curves are shown in Fig. 6 for dodecane. The temperature range used for the EOS parameters fitting was 300–500 K. It appears clearly that inside this range the agreement between theoretical and experimental curves is excellent. Out of this range, in particular close to the critical point, the accuracy decreases. Another temperature range may be chosen when a better accuracy is required for higher temperatures. For the present applications, the temperature range 300–500 K is appropriate enough and we shall never deal with thermodynamic conditions close to the critical point.

In the next section, the resolution of the reactive Riemann problem associated to evaporation fronts is detailed using 'Stiffened Gas' EOS.

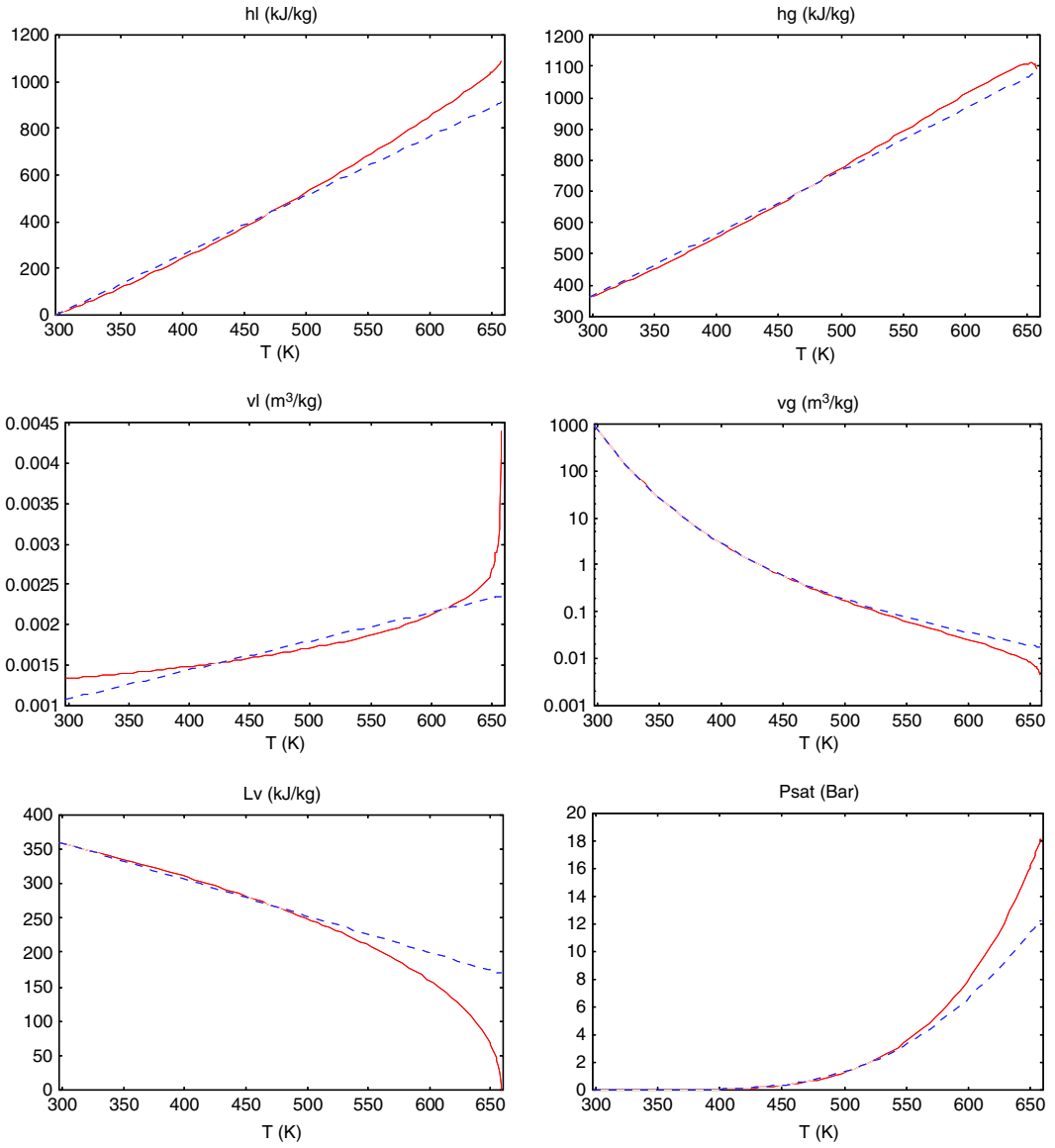

Fig. 6. Experimental (lines) and theoretical (dotted lines) saturation curves for liquid and vapor dodecane. Theoretical curves are obtained using pure fluid 'Stiffened Gas' EOS.

3. The reactive Riemann problem for the Euler equations

In this section, the solution of the reactive Riemann problem is established for the one-dimensional mixture Euler equations. The mixture Euler equations are used because the evaporation front separates a pure liquid from a liquid–vapor mixture under thermodynamic equilibrium.

The Riemann problem is of fundamental importance concerning the numerical strategy developed for the multi-dimensional front propagation.

Before dealing with the reactive Riemann problem, we recall the basis of a conventional Riemann solver for the Euler equations. The reactive Riemann solver shall use the same ingredients, completed by additional relations associated to the evaporation front.

3.1. Recalls on the inert Riemann problem

The inert Riemann problem associated to the Euler equations is given by:

$$\begin{cases} \frac{\partial U(x,t)}{\partial t} + \frac{\partial F(U(x,t))}{\partial x} = 0, \\ U(x,0) = \begin{cases} U_{\mathrm{L}} \text{ if } x < 0, \\ U_{\mathrm{R}} \text{ if } x > 0, \end{cases} \end{cases} \tag{10}$$

where $U(x,t) = (\rho,\rho u,\rho E)^{\mathrm{T}}$ and $F(U(x,t)) = (\rho u,\rho u^2 + P,(\rho E + P)u)^{\mathrm{T}}$.

U_{L} and U_{R} are constant initial states. ρ, u and P are, respectively, the density, the material velocity and the pressure. The total energy is defined as $E = e + 1/2u^2$, where e is the internal energy. The system (10) is closed by the 'Stiffened Gas' EOS given by relation (1).

The problem (10) consists in finding the intermediate constant states U_{L}^* and U_{R}^* delimited by the various waves (expansions, shocks or contact discontinuities) present in the medium.

The different jump relations available across the various waves are of three types: Riemann invariants (isentropic relations) for rarefaction waves, Rankine–Hugoniot relations for shock waves and interface conditions for the contact discontinuity u.

Across this one, the interface conditions are $u = cst$ and $P = cst$.

Across rarefaction waves, the isentropic relations are:

$$u = u_0 \pm \frac{2c_0}{\gamma - 1}\left(\left(\frac{P + P_\infty}{P_0 + P_\infty}\right)^{(\gamma-1)/2\gamma} - 1\right) \tag{11a}$$

$$\rho = \rho_0\left(\frac{P + P_\infty}{P_0 + P_\infty}\right)^{1/\gamma} \tag{11b}$$

with ± for right- and left-facing expansion waves, respectively. The state with subscript 0 is the state in which rarefaction waves propagate.

The Rankine–Hugoniot relations are given by:

$$u = u_0 + m\left(\frac{1}{\rho_0} - \frac{1}{\rho}\right), \tag{12a}$$

$$P = P_0 + m^2\left(\frac{1}{\rho_0} - \frac{1}{\rho}\right), \tag{12b}$$

$$e = e_0 + \frac{P + P_0}{2}\left(\frac{1}{\rho_0} - \frac{1}{\rho}\right), \tag{12c}$$

where $m = \rho_0(\sigma - u_0)$ represents the mass flow rate (σ is the shock speed) and the state with subscript 0 is the state in which the shock propagates. Using the 'Stiffened Gas' EOS (1), system (12) writes:

$$u = u_0 \pm \frac{P - P_0}{\rho_0 c_0 \sqrt{\frac{\gamma+1}{2\gamma}\left(\frac{P+P_\infty}{P_0+P_\infty}\right) + \frac{\gamma-1}{2\gamma}}}, \tag{13a}$$

$$m^2 = (\rho_0 c_0)^2 \left(\frac{\gamma+1}{2\gamma} \left(\frac{P+P_\infty}{P_0+P_\infty} \right) + \frac{\gamma-1}{2\gamma} \right), \tag{13b}$$

$$\rho = \rho_0 \frac{(\gamma+1)\left(\frac{P+P_\infty}{P_0+P_\infty}\right)+\gamma-1}{(\gamma-1)\left(\frac{P+P_\infty}{P_0+P_\infty}\right)+\gamma+1}, \tag{13c}$$

with ± for right- and left-facing shock waves, respectively.

Thus, relations (11a) and (13a) write under the same form:

$$u = u_0 \pm \phi_0(P), \tag{14}$$

with

$$\phi_0(P) = \begin{cases} \dfrac{P-P_0}{\rho_0 c_0 \sqrt{\frac{\gamma+1}{2\gamma}\left(\frac{P+P_\infty}{P_0+P_\infty}\right)+\frac{\gamma-1}{2\gamma}}} & \text{if } P > P_0, \\ \dfrac{2c_0}{\gamma-1}\left(\left(\frac{P+P_\infty}{P_0+P_\infty}\right)^{\frac{\gamma-1}{2\gamma}} - 1 \right) & \text{otherwise.} \end{cases} \tag{15}$$

Now substituting subscript 0 in (14) and (15) by subscripts L and R corresponding to the left and right states, respectively, we get:

$$u^* = u_L - \phi_L(P^*), \tag{16}$$

$$u^* = u_R + \phi_R(P^*), \tag{17}$$

where the interface conditions $u_L^* = u_R^* = u^*$ and $P_L^* = P_R^* = P^*$ have been used.

Thus, the combination of (16) and (17) leads to a scalar equation:

$$F(P^*) = u_R - u_L + \phi_R(P^*) + \phi_L(P^*) = 0. \tag{18}$$

The solution of (18) is obtained by using an iterative numerical method (Newton–Raphson for example). Once the pressure P^* is obtained, the other flow variables are calculated from the appropriate relations given previously. More details about the resolution of the inert Riemann problem are described for example in [9,18,25,37]. An example of solution obtained by such solver is provided hereafter.

An initial velocity discontinuity is located at the middle of a 1-m length tube. The velocities are initially −500 m/s at the left and +500 m/s at the right. The domain contains a liquid at atmospheric pressure whose density is $\rho = 1000$ kg/m^3. The EOS parameters are $\gamma = 4.4$ and $P_\infty = 6 \times 10^8$ Pa.

This symmetric problem appears for example in the treatment of wall boundary conditions used in Godunov type schemes. The solution, represented at time $t = 200$ μs in Fig. 7, consists in two symmetric rarefaction waves propagating to the left and to the right. At the middle of the domain, the velocity is zero while the pressure decreases to negative values. Even at such pressure levels, the sound speed is defined because the term $(P + P_\infty)$ remains positive. This solution is not physically acceptable. Indeed, through a strong expansion wave, the liquid reaches a thermodynamic state inside the saturation dome: it becomes superheated. Then the liquid transforms into vapor in order to reach an equilibrium state at positive pressure. These effects are taken into account in the next part.

3.2. The reactive Riemann problem

Isentropic and shock relations described in the previous part are used again in the reactive Riemann problem but are only valid among pure fluids. The physical phenomenon we have to describe (Fig. 1) leads

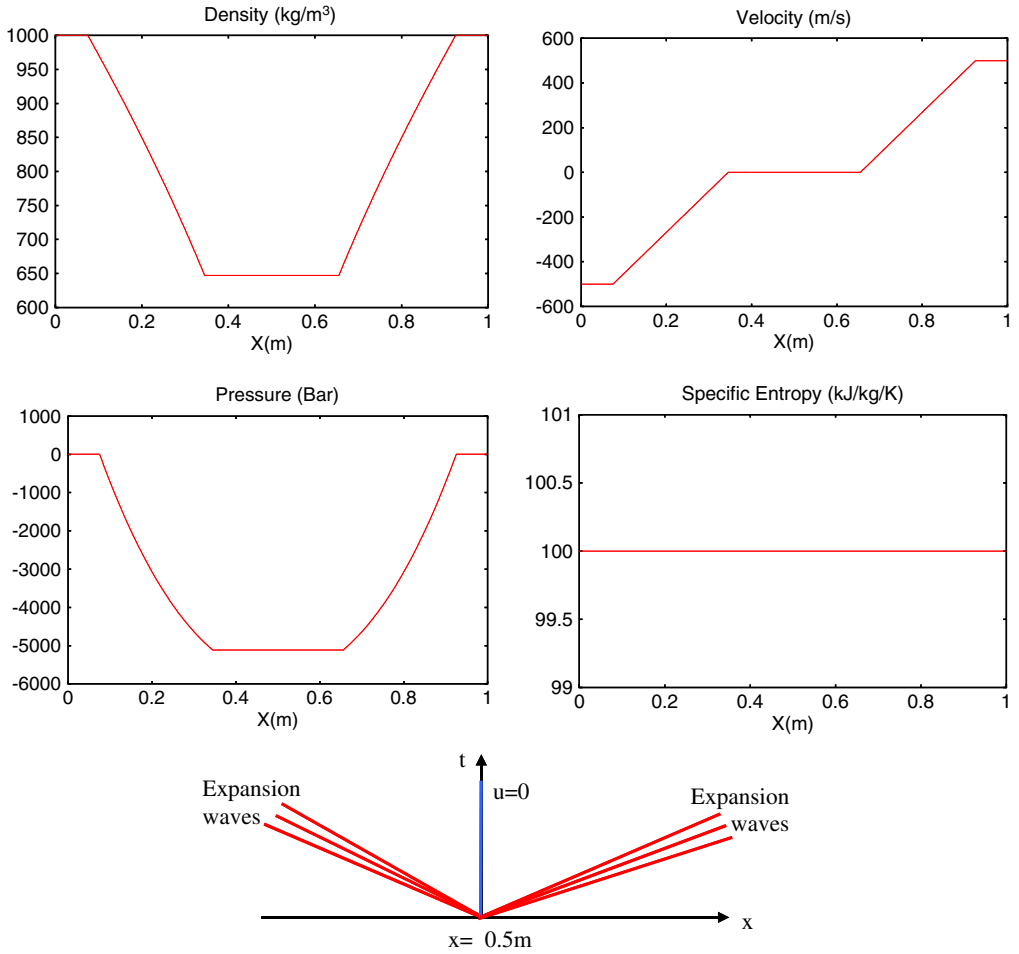

Fig. 7. Exact solution of the inert Riemann problem associated to the expansion tube.

to an additional front through which vapor appears. Such reactive fronts are described in [9,11,18,35] for example. Like any discontinuity, this front obeys the Rankine–Hugoniot relations (12). But, contrary to classical shocks, the EOS parameters are different on both sides of the front. In addition, as reported in Section 1, a kinetic relation must complete the Rankine–Hugoniot relations.

3.2.1. Available relations across reactive fronts

The thermodynamic behavior of the superheated liquid (subscript 0) obeys:

$$e_0(P_0,\rho_0) = \frac{P_0 + \gamma_0 P_{\infty 0}}{(\gamma_0 - 1)\rho_0} + q_0. \tag{19}$$

While the appearing fluid (vapor) obeys:

$$e(P,\rho) = \frac{P + \gamma P_\infty}{(\gamma - 1)\rho} + q. \tag{20}$$

Here, we assume a total evaporation. We shall examine later the case where a mixture appears behind the front. Combining relations (12c), (19) and (20), we obtain:

$$\rho = \rho_0 \frac{\frac{\gamma+1}{\gamma-1}(P+P_\infty)+P_0+P_\infty}{\frac{\gamma_0+1}{\gamma_0-1}(P_0+P_{\infty 0})+P+P_{\infty 0}-2\rho_0\Delta q}, \tag{21}$$

where $\Delta q = q - q_0$ denotes the difference between reference energies. The relation (21) represents the Crussard curve relative to the initial state (ρ_0, P_0). This curve (see Fig. 8) is divided in three parts. One of them (dotted lines) is a non-physical area because it corresponds to positive slopes ($m^2 < 0$) of the Rayleigh line represented by relation (12b). Two points delimit this non-admissible area. The first one corresponds to a constant pressure deflagration ($P = P_0$) whose associated density is given by:

$$\rho_p = \frac{\gamma(P_0+P_\infty)}{\frac{\gamma-1}{\gamma_0-1}c_0^2-(\gamma-1)\Delta q} < \rho_0. \tag{22}$$

The second point corresponds to a constant volume explosion ($\rho = \rho_0$) whose associated pressure reads:

$$P_v = \frac{\gamma-1}{\gamma_0-1}(P_0+\gamma_0 P_{\infty 0})-\gamma P_\infty-(\gamma-1)\rho_0\Delta q > P_0. \tag{23}$$

The upper part of the Crussard curve in Fig. 8 corresponds to the detonation branch ($P > P_v$) while the lower part represents the deflagration branch ($P < P_0$). The detonation branch cannot be reached because vapor appearance would be non-sense in this case. Indeed this zone corresponds to situations where compression waves are present in the medium, bringing the liquid back to a non-superheated state. Consequently, the solution locates in the deflagration area: the evaporation front is undercompressive.

Now, combining relations (12b) and (21) the mass flow rate read:

$$m^2 = \frac{\rho_0}{2}((\gamma+1)(P+P_\infty)+(\gamma-1)(P_0+P_\infty))\frac{P-P_0}{P-P_v}. \tag{24}$$

The combination of relations (12a), (12b) and (24) gives the following material velocity expression:

$$u = u_0 \pm sg(P-P_0)\sqrt{\frac{2(P-P_0)(P-P_v)}{\rho_0((\gamma+1)(P+P_\infty)+(\gamma-1)(P_0+P_\infty))}} \tag{25}$$

with ± for a right(left)-facing front, respectively.

Nevertheless, all the relations above are valid when the evaporation is total. Such situation occurs when the degree of superheat is high and the latent heat of vaporization is small enough. But in some cases these two conditions are not satisfied (see [33] for example). In this case, a liquid–vapor mixture at equilibrium (thermodynamically and cinematically) appears behind the front. Thus, the associated thermodynamic state lies inside the saturation dome and belongs to the mixture Crussard curve we detail hereafter.

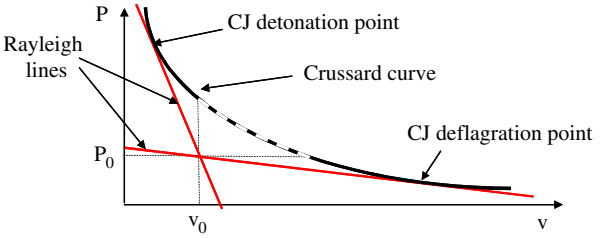

Fig. 8. Crussard curve and Rayleigh line in a (P,v) diagram associated to a superheated liquid state (subscript 0).

Such a mixture is governed by the homogeneous Euler equations:

$$\frac{\partial U(x,t)}{\partial t}+\frac{\partial F(U(x,t))}{\partial x}=0, \tag{26}$$

where $U(x,t)=(\rho,\rho u,\rho E)^{\mathrm{T}}$ and $F(U(x,t))=(\rho u,\rho u^2+P,(\rho E+P)u)^{\mathrm{T}}$. Here ρ represents the mixture density $\rho=(\alpha\rho)_{\mathrm{g}}+(\alpha\rho)_{\mathrm{l}}$ and $e=E-1/2u^2$ is the mixture internal energy defined as $\rho e=(\alpha\rho e)_{\mathrm{g}}+(\alpha\rho e)_{\mathrm{l}}$, where α_k is the volume fraction of the phase k (k = g,l). Each phase EOS $e_k(P,T)$ and $\rho_k(P,T)$, given by relations (2) and (3), are also used. Assuming that liquid and vapor are in thermodynamic equilibrium, we use the saturation curve $T(P)$ given by relation (7). Then, each phase EOS only depend on the pressure P, $e_k(P)$ and $\rho_k(P)$.

The mixture variables read:

$$\begin{cases}\rho=\rho_{\mathrm{l}}+\alpha_{\mathrm{g}}(\rho_{\mathrm{g}}-\rho_{\mathrm{l}})=\rho(P,\alpha_{\mathrm{g}}),\\ e=\frac{1}{\rho}\left(\rho_{\mathrm{l}}e_{\mathrm{l}}+\alpha_{\mathrm{g}}(\rho_{\mathrm{g}}e_{\mathrm{g}}-\rho_{\mathrm{l}}e_{\mathrm{l}})\right)=e(\rho,P,\alpha_{\mathrm{g}}).\end{cases} \tag{27}$$

Combining relations of system (27), the mixture EOS reads:

$$e(\rho,P)=\frac{1}{\rho}\left(\rho_{\mathrm{l}}e_{\mathrm{l}}+\frac{\rho-\rho_{\mathrm{l}}}{\rho_{\mathrm{g}}-\rho_{\mathrm{l}}}(\rho_{\mathrm{g}}e_{\mathrm{g}}-\rho_{\mathrm{l}}e_{\mathrm{l}})\right). \tag{28}$$

By using the definition of the sound speed $c^2=\left(\frac{\partial P}{\partial\rho}\right)_s=\frac{\left(\frac{P}{\rho^2}-\frac{\partial e}{\partial\rho}\right)_P}{\left(\frac{\partial e}{\partial P}\right)_\rho}$ and the mixture EOS (28), we obtain the following relation:

$$\frac{1}{\rho c^2}=\frac{\alpha_{\mathrm{g}}}{\rho_{\mathrm{g}}c_{\mathrm{g}}^2}+\frac{\alpha_{\mathrm{l}}}{\rho_{\mathrm{l}}c_{\mathrm{l}}^2}+T\left(\frac{\alpha_{\mathrm{g}}\rho_{\mathrm{g}}}{C_{P,g}}\left(\frac{\mathrm{d}s_{\mathrm{g}}}{\mathrm{d}P}\right)^2+\frac{\alpha_{\mathrm{l}}\rho_{\mathrm{l}}}{C_{P,\mathrm{l}}}\left(\frac{\mathrm{d}s_{\mathrm{l}}}{\mathrm{d}P}\right)^2\right), \tag{29}$$

where $C_{P,\mathrm{g}}$ and $C_{P,\mathrm{l}}$ are heat capacities at constant pressure of both phases and $\frac{\mathrm{d}s_{\mathrm{g}}}{\mathrm{d}P}$, $\frac{\mathrm{d}s_{\mathrm{l}}}{\mathrm{d}P}$ are derivatives along the saturation curve $T(P)$. In relation (29), the term $\frac{\alpha_{\mathrm{g}}}{\rho_{\mathrm{g}}c_{\mathrm{g}}^2}+\frac{\alpha_{\mathrm{l}}}{\rho_{\mathrm{l}}c_{\mathrm{l}}^2}\overset{\text{def}}{=}\frac{1}{\rho c_{\mathrm{w}}^2}$ is the Wood formula [39] representing the mixture sound speed where only pressure equilibrium between phases is considered.

Thus the mixture sound speed c is defined since c_{g} and c_{l} are defined. In addition, the mixture EOS (28) is convex. Indeed, an EOS is convex if $c^2\geqslant 0$ and $\frac{c^2}{v^2}\left(\frac{\partial T}{\partial s}\right)_v\geqslant\left[\left(\frac{\partial P}{\partial s}\right)_v\right]^2$. In our case, the first condition is fulfilled by relation (29). Now using the saturation curve $T(P)$, we have $\left(\frac{\partial T}{\partial s}\right)_v=\frac{\mathrm{d}T}{\mathrm{d}P}\left(\frac{\partial P}{\partial s}\right)_v$ and $\frac{c^2}{v^2}\frac{\mathrm{d}T}{\mathrm{d}P}=\left(\frac{\partial P}{\partial s}\right)_v$. Then the second condition is fulfilled too.

We now detail the building of the mixture Crussard curve lying inside the saturation dome. Such a liquid–vapor mixture obeying the homogeneous Euler equations (26), the Rankine–Hugoniot relations (12) remain unchanged. Combining relations (27) and (12c), we obtain:

$$\alpha_{\mathrm{g}}(P)=\frac{e_0-e_{\mathrm{l}}+\frac{P+P_0}{2}\left(\frac{1}{\rho_0}-\frac{1}{\rho_{\mathrm{l}}}\right)}{e_0-e_{\mathrm{l}}+\frac{P+P_0}{2}\left(\frac{1}{\rho_0}-\frac{1}{\rho_{\mathrm{l}}}\right)-\frac{\rho_{\mathrm{g}}}{\rho_{\mathrm{l}}}\left(e_0-e_{\mathrm{g}}+\frac{P+P_0}{2}\left(\frac{1}{\rho_0}-\frac{1}{\rho_{\mathrm{g}}}\right)\right)}. \tag{30}$$

Then the mixture density obeys the relation:

$$\rho(P)=\rho_{\mathrm{l}}+\alpha_{\mathrm{g}}(P)(\rho_{\mathrm{g}}-\rho_{\mathrm{l}}), \tag{31}$$

whose curve in a (P,v) diagram is the mixture Crussard curve represented in Fig. 9, only valid inside the saturation dome.

In brief, whatever the medium behind the front is (pure vapor or liquid–vapor mixture), the available relations across the front are the Rankine–Hugoniot relations (12) associated to the Euler equations (26).

It is important to note the presence of two particular points in Figs. 8 and 9. These are tangential points of the Rayleigh line and the Crussard curve. The high-pressure solution ($P>P_v$) and the low-pressure solu-

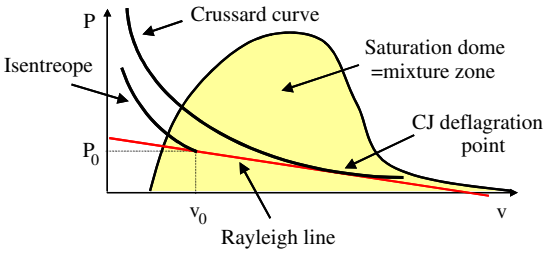

Fig. 9. Mixture Crussard curve and Rayleigh line in a (P,v) diagram associated to a superheated liquid state (subscript 0).

tion ($P < P_0$) are named, respectively, the Chapman–Jouguet detonation and deflagration points (CJ points).

3.2.2. Properties of the Chapman–Jouguet points

Geometrically (see Fig. 8), these points are characterized by $\frac{dP}{d\rho} = \frac{m^2}{\rho^2}$ (the derivative of the Crussard curve coincides with the slope of the Rayleigh line).

Differentiation of the Rayleigh line equation (12b) yields to:

$$dP = \frac{m^2}{\rho^2}\, d\rho + \left(\frac{1}{\rho_0} - \frac{1}{\rho}\right) dm^2. \tag{32}$$

Then, from (32) we deduce that $dm^2/dP = 0$ at these particular points. Indeed, at the CJ detonation (deflagration) point, the slope of the Rayleigh line ($-m^2$) is locally a maximum (minimum). Consequently, the mass flow rate m and the speed of the front D are locally minima (maxima). In addition, it can be shown that specific entropy is locally a minimum (maximum) at the CJ detonation (deflagration) point [11,18]. Since $ds = 0$, we can use the equivalent relation $dP = c^2 d\rho$ to obtain:

$$m^2 = \rho^2 c^2 \iff D = u \pm c, \tag{33}$$

with ± for right(left)-facing fronts, respectively.

When only pure vapor is produced across the front, the CJ points may be determined explicitly. Indeed, with the help of the 'Stiffened Gas' EOS, relation (33) becomes:

$$m^2 = \gamma\rho(P + P_\infty). \tag{34}$$

Combining relations (12b), (21) and (34), we obtain a second-order equation in P:

$$P^2 - 2P_v P + P_0^2 + 2(P_0 - P_v)\frac{\gamma P_\infty - P_0}{\gamma + 1} = 0. \tag{35}$$

The two solutions of (35) are the pressures associated to CJ points:

$$P_{CJ} = P_v \pm \sqrt{(P_v - P_0)\left(P_v + P_0 + \frac{2}{\gamma + 1}(\gamma P_\infty - P_0)\right)}, \tag{36}$$

with ± for the CJ detonation (deflagration) point, respectively.

Now, when CJ deflagration point corresponds to a thermodynamic mixture state, as represented in Fig. 9, the previous explicit calculations cannot be achieved. In this case, we use another property of the CJ point, that is $dm^2/dP = 0$ along the mixture Crussard curve for $P < P_0$.

The combination of (12b) and (31) gives the following relation:

$$m^2(P) = \frac{P - P_0}{\frac{1}{\rho_0} - \frac{1}{\rho(P)}}. \tag{37}$$

Derivation of the expression (37) with respect to the pressure P leads to:

$$\frac{\mathrm{d}m^2}{\mathrm{d}P} = 0 \iff \frac{\rho_0}{\rho(P)} \frac{\mathrm{d}\rho(P)}{\mathrm{d}P} - \frac{\rho(P) - \rho_0}{P - P_0} = 0. \tag{38}$$

The term $\mathrm{d}\rho(P)/\mathrm{d}P$ is obtained by successive derivations of the different variables $e_k(P)$ and $\rho_k(P)$ in relations (30) and (31). The value of the CJ deflagration pressure is thus obtained by a numerical procedure to solve Eq. (38). Such procedure is preferred to the use of the mixture sound speed (29). It can be noticed that convexity of the mixture EOS examined before implies the existence of CJ points.

3.2.3. Waves patterns in the reactive Riemann problem

As the evaporation front is subsonic with respect to the medium in which it propagates, it is preceded by a precursor wave (shock or expansions) propagating approximately at the liquid sound speed, as represented in Fig. 1. By enumerating the various unknowns (pressure, density and flow velocity for each intermediate state and two wave speeds: shock and evaporation front) and the available relations (three Rankine–Hugoniot relations for shock and evaporation front, two relations for expansion waves and contact discontinuity), we have 11 unknowns and 10 relations. The kinetic relation that controls the phase change rate achieves the Riemann problem closure. In the rest of the paper, we adopt the CJ deflagration kinetic relation, for evaporation problems.

This kinetic relation may be understood by the following interpretations. This one corresponds to a maximal entropy jump across the front and a maximal front velocity. Thus, it is not a stable point contrary to the CJ detonation point. It can be seen as the maximal mass flow rate that cannot be overstepped. For example, in low combustion phenomena, the front stability is due to thermal diffusion. Nevertheless, the mass flow rate and the front velocity cannot exceed the ones associated to the CJ deflagration limit. This is exactly the same case for evaporation fronts. These ones appear as a consequence of liquid expansion. The pressure drop in the liquid through expansion waves increases when the initial pressure ratio increases too, as well as the metastable character of the superheated liquid. As the system tends to relax as fast as possible towards equilibrium, we observe microscopic interface instabilities that tend to maximize front area in order to reach the maximum mass flow rate.

At the macroscopic scale, where the front is considered as a discontinuity, the effects related to the increase of front area have magnified the local mass flow rate. Thus the CJ condition appears as a macroscopic kinetic relation involving both effects of local mass flow rate and multi-dimensional effects that tend to maximize front area. The CJ kinetic relation consists in a global (by opposition to local) relation that summarizes multi-dimensional instabilities.

In brief, for both situations of partial or total evaporation, the front is always preceded by a precursor wave. During the resolution of the reactive Riemann problem, we designate by 'composite wave' the waves group composed of the precursor and the CJ deflagration front. The precursor could be compressive or undercompressive according to the pressure behind the front as represented in Fig. 10.

3.2.4. Resolution of the reactive Riemann problem

The resolution depends on a liquid 'reactivity factor'. This factor expresses the fact that the liquid may change phase or not. First, an inert resolution is done like in the previous subsection. Then, we compare the solution P^* with the associated saturated pressure $P_{\mathrm{sat}}(T^*)$, where T^* is the liquid temperature.

If $P^* > P_{\mathrm{sat}}(T^*)$, the liquid is not superheated and does not transform into vapor. In this case, the Riemann problem remains inert. If $P^* < P_{\mathrm{sat}}(T^*)$ then the liquid is superheated (thermodynamic state inside

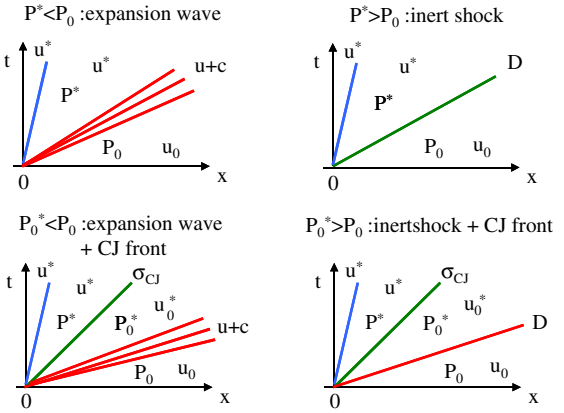

Fig. 10. Waves patterns in the reactive Riemann problem associated to evaporation fronts.

the saturation dome). In this case, we have to solve the associated reactive Riemann problem. This one is solved using an iterative method, like in the inert case. At each iteration, the pressure P^* determines the waves pattern (simple or composite waves) that must be considered so as to connect the state associated to P^* to the left and right states denoted by subscripts L and R.

Let us recall that in the inert case, two instances are possible:

- if $P^* \geqslant P_0$, the wave corresponds to a shock and we use the Rankine–Hugoniot relations (13),
- if $P^* \leqslant P_0$, the wave is an expansion and we use the isentropic relations (11).

If the fluid is a liquid, a CJ deflagration front connects the CJ state P^* to an intermediate state 0* (superheated liquid). This front is preceded by the precursor wave connecting the state 0* and the initial state 0 of the liquid. Then two cases are possible to connect the states 0* and 0:

- if $P_0^* > P_0$, the precursor is a shock and we use the relations (13),
- if $P_0^* \leqslant P_0$, the precursor is an expansion wave and we use the relations (11).

The relations associated to the previous waves patterns can be written under a common form:

$$u^* = u_0 \pm \phi_0(P^*), \tag{39}$$

with

$$\phi_0(P^*) = \begin{cases} \dfrac{P^* - P_0}{\rho_0 c_0 \sqrt{\frac{\gamma_0+1}{2\gamma_0}\left(\frac{P^*+P_{\infty 0}}{P_0+P_{\infty 0}}\right)+\frac{\gamma_0-1}{2\gamma_0}}} & \text{if } P^* > P_0 \text{ (inert)}, \\ \dfrac{2c_0}{\gamma_0-1}\left(\left(\dfrac{P^*+P_{\infty 0}}{P_0+P_{\infty 0}}\right)^{(\gamma_0-1)/2\gamma_0} - 1\right) & \text{if } P^* \leqslant P_0 \text{ (inert)}, \\ u_0^* - u_0 + \dfrac{P^* - P_0^*}{m_{\mathrm{CJ}}(P^*)} & \text{(reactive)}, \end{cases} \tag{40}$$

where $m_{\mathrm{CJ}}(P^*)$ is the CJ mass flow rate through the reactive front with respect to the state 0*.

This one is calculated so that the pressure P^* coincides exactly to the CJ deflagration pressure. For each value of P^*, a unique associated state 0* is obtained by an iterative method we detail hereafter.

For each value of P_0^*, the associated density is given by:

$$\rho_0^* = \begin{cases} \rho_0 \dfrac{(\gamma_0+1)\left(\frac{P_0^*+P_{\infty 0}}{P_0+P_{\infty 0}}\right)+\gamma_0-1}{(\gamma_0-1)\left(\frac{P_0^*+P_{\infty 0}}{P_0+P_{\infty 0}}\right)+\gamma_0+1} & \text{if } P_0^* > P_0, \\ \rho_0 \left(\dfrac{P_0^*+P_{\infty 0}}{P_0+P_{\infty 0}}\right)^{1/\gamma_0} & \text{otherwise,} \end{cases} \tag{41}$$

Then the density ρ_{CJ} and the mass flow rate m_{CJ} are obtained either by relations (21) and (34) in the total evaporation case or relations (31), (37) and (38) in the partial evaporation case.

Then we use the Rayleigh line equation (12b) to update P_0^* at each iteration:

$$P_0^* = P^* - m_{CJ}^2\left(\frac{1}{\rho_0^*} - \frac{1}{\rho_{CJ}}\right). \tag{42}$$

The value of P_0^* is then modified until convergence is obtained. The other variables associated to the state 0* are determined either by relations (13) or by relations (11) in accordance with P_0^*.

Now substituting subscript 0 in (39) and (40) by subscripts L and R corresponding to the left and right states, respectively, we get:

$$u^* = u_L - \phi_L(P^*), \tag{43}$$

$$u^* = u_R + \phi_R(P^*). \tag{44}$$

Combining relations (43) and (44), a scalar equation is recovered:

$$F(P^*) = u_R - u_L + \phi_R(P^*) + \phi_L(P^*) = 0. \tag{45}$$

The solution P^* is determined again by an iterative method (Newton–Raphson for example). Once P^* is obtained, the waves patterns and the whole solution of the reactive Riemann problem are uniquely determined.

3.2.5. Examples of reactive Riemann problem solutions

We present here two examples of reactive Riemann problem solutions. The first one is dealing with a total evaporation front while the second one is dealing with a partial evaporation front. In all cases, the different phases are liquid dodecane and its vapor whose EOS parameters are given in Section 2.

In the first example, a liquid at atmospheric pressure with density $\rho = 600$ kg/m^3 (right) is connected to a low-pressure chamber $P = 100$ Pa (left) filled with gaseous dodecane whose density is $\rho = 10^{-4}$ kg/m^3. Initially the medium is at rest. The initial discontinuity is located at $x = 0.5$ m in a 1-m length tube.

The exact solution is represented at time $t = 370$ μs in Fig. 11. It consists in a shock wave propagating towards the low-pressure chamber and an expansion wave propagating into the initial liquid. This one becomes superheated and is travelled by the evaporation front at low speed. In the pressure graph, the rarefaction waves look like a discontinuity because the liquid sound speed is much larger than material velocity.

In the second example, a 1-m length tube is filled with liquid dodecane at atmospheric pressure and density $\rho = 600$ kg/m^3. An initial material velocity is located at $x = 0.5$ m. On the left, the velocity is set to $u = -100$ m/s and on the right, $u = +100$ m/s. The exact solution of this symmetric problem is represented at time $t = 300$ μs in Fig. 12. It consists in left and right-facing rarefaction waves propagating into the liquid on both sides of the initial velocity discontinuity. Two partial evaporation fronts propagate towards the superheated liquid. This last example is of fundamental importance for cavitation as mentioned previously in the inert case. Indeed, wall boundary conditions use fictitious cells corresponding to such Riemann problem. This example explains why cavitation pockets may appear in multi-dimensional flows at geometrical singularities.

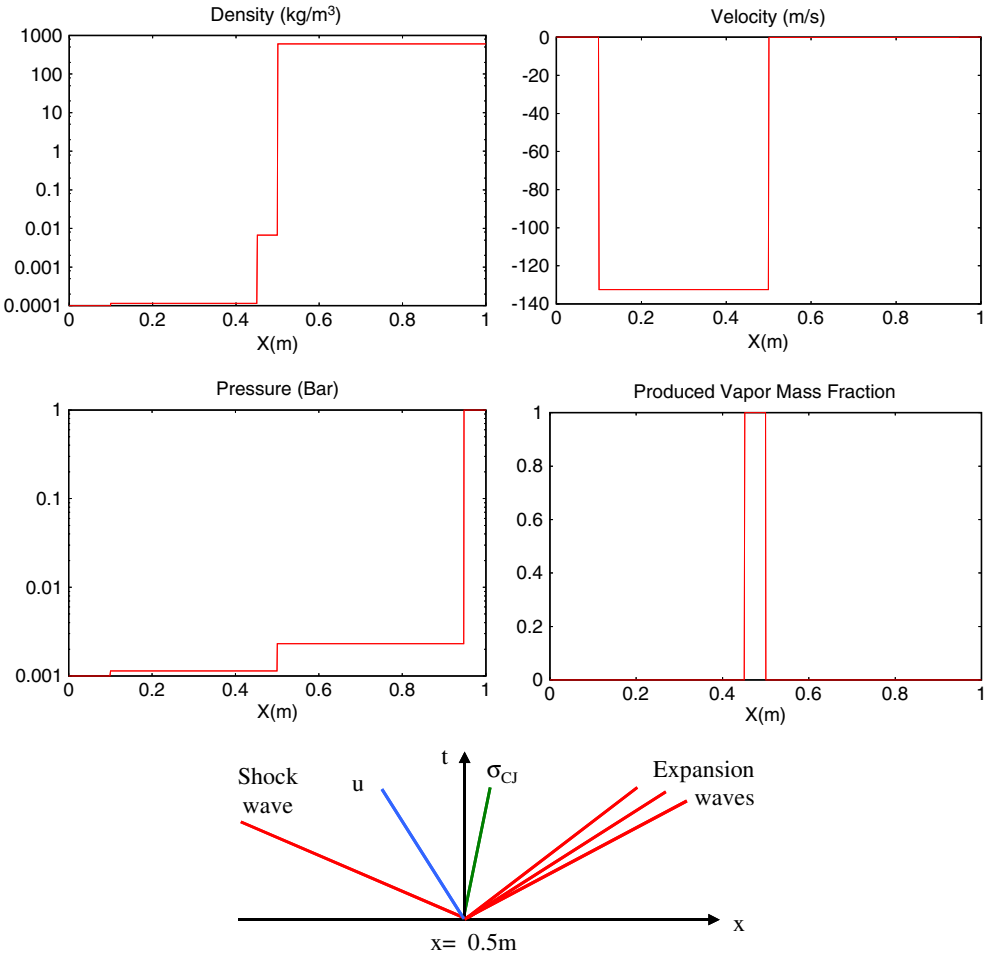

Fig. 11. Exact solution of the liquid–vapor expansion tube with an evaporation front.

The waves mechanism has been introduced in the reactive Riemann problem. The amplitude of expansion waves in cavitating flows is so high that the use of the CJ deflagration kinetic relation is justified. Nevertheless, in more general situations, evaporation front does not always obey this limit kinetic law. Indeed, the mass flow rate through the reactive front may not be a maximum, like in very low phenomena based on diffusive effects with large characteristic time scales. In this case, thermal diffusion must be considered as well as capillary effects for the determination of an appropriate kinetic law. Such a kinetic law can be obtained by the study of travelling waves of the Euler equations augmented by thermal diffusion or other capillary model as in [14]. This work is actually in progress. Once the kinetic relation is determined, it would be quite easy to replace the CJ deflagration law by such relation in the present reactive Riemann solver. For now, we restrict the applications to cavitating flows and adopt the CJ kinetic relation.

The next issue is the second challenge of this work. It consists in the two-dimensional propagation of the subsonic evaporation front. To our knowledge, there is no method able to deal with such an issue. Some success has been obtained in one dimension with the random choice method [17,9] and the works of [22] because the composite waves are correctly handled by such methods. In two dimensions, as we do not want

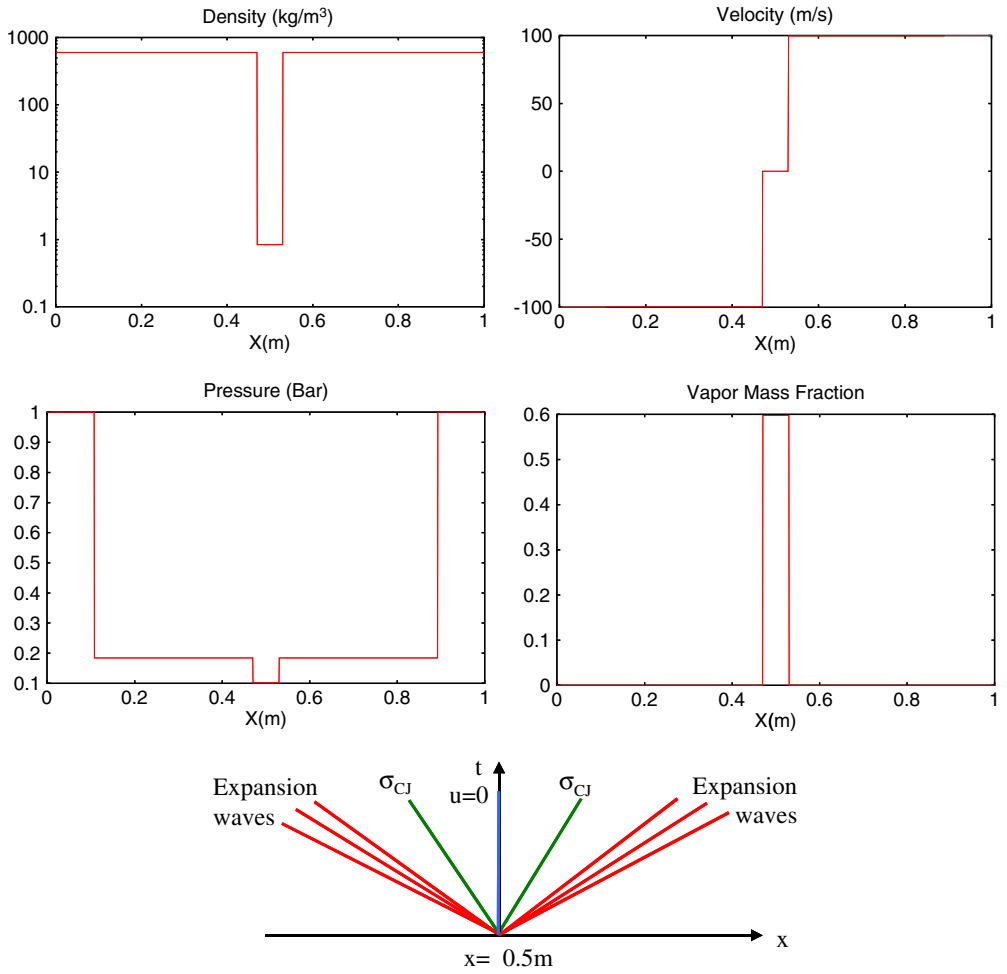

Fig. 12. Exact solution of the symmetric reactive expansion tube.

to compute the front structure as done usually with flames, we need a method able to propagate a subsonic discontinuity with composite features. In the next section, we reach this goal by extending the discrete equations method (DEM) [2,29,8].

4. Implementation of the reactive Riemann solver into the discrete equations method (DEM)

In order to treat multi-dimensional propagation of evaporation fronts, we extend in this section the numerical method named DEM (discrete equations method), recently proposed by [2,29,8] for interface problems and multiphase mixtures. This method consists in connecting several systems of equations, each one being associated to a pure fluid. It leads to discrete equations that can be used for interface problems or multiphase flows with several velocities. It may be considered as an homogenization method belonging to the class of averaging methods.

Usually, multiphase flows equations are obtained by mathematical averaging procedures [12]. Another option is based on the Hamilton principle as given in [16] for example. Both methods yield to non-conservative systems where average interfacial variables appear [30]. In all cases, the resulting system must be solved by numerical approximations. In this kind of approach, the determination of the average variables as well as the numerical approximation of the non-conservative terms is always questionable.

These difficulties are solved by the present method. Contrary to conventional methods, the averaged equations for the mixture are not used. Interface problems between pure fluids are solved locally with the help of their own governing equations. In [2], it was done with the Euler equations for each fluid resulting in interface problem solution obtained with conventional Riemann solver. In [29], a turbulent flow model was used in each fluid with the associated Riemann problem solution. The local interface variables are determined at each interface of the two-phase flow mixture whose topology is given a priori. Then, an averaging procedure is applied over all these solutions. In that sense, it proceeds like a conventional Godunov scheme. The averaged interface solutions provide a set of discrete equations that can be used directly as a numerical scheme. Their continuous limit was obtained in [29] and identified to the Baer–Nunziato model [5] with more general closure relations for averaged interface variables.

In the present paper, we use the discrete equations method as a numerical scheme to propagate permeable fronts. Nevertheless, important extensions are necessary since the reactive Riemann problem built in Section 3 is used. This is the main topic of this section. We shall see that this method is able to treat correctly the non-conservative terms and to take into account all waves present in the medium including reactive fronts. Moreover, this method is absolutely necessary to solve special features of subsonic fronts as reported in introduction.

In the following, we first recall the basis of this method for two inert fluids. We then extend the method to reacting fluids with permeable fronts. Additional terms (reactive fluxes) appear and modifications of the Eulerian and Lagrangian fluxes introduced in [2,29] are necessary.

4.1. Recalls on the discrete equations method for inert fluids

For any type of two-phase mixture (liquid drops into a gas, gas bubbles into a liquid, separated and annular flows) as well as flows with macroscopic interfaces, each pure fluid is assumed to obey the Euler equations. They interact via their interfaces at the microscopic scale when dealing with mixtures and at macroscopic scale when dealing with interface problems. The averaging of the various interactions inside a two phase control volume yield couplings between the two fluids that appear as macroscopic variables like the volume fraction and non-conservative terms or Lagrangian fluxes as introduced in [2,29,8]. In the following, we summarize this method considering only a separated flow topology.

The interfaces under study evolving in two dimensions, each pure fluid obeys the 2D Euler equations:

$$\frac{\partial U}{\partial t}+\frac{\partial F}{\partial x}+\frac{\partial G}{\partial y}=0, \tag{46}$$

where $U=[1,\ \rho,\ \rho u,\ \rho v,\ \rho E]^{\mathrm{T}}$, $F=[0,\ \rho u,\ \rho u^2+P,\ \rho uv,\ (\rho E+P)u]^{\mathrm{T}}$ and $G=[0,\ \rho v,\ \rho uv,\ \rho v^2+P,\ (\rho E+P)v]^{\mathrm{T}}$.

The first trivial equation $\frac{\partial 1}{\partial t}+\frac{\partial 0}{\partial x}+\frac{\partial 0}{\partial y}=0$ comes from an evolution equation expressing the link between the Lagrangian and Eulerian coordinates. This trivial identity will be necessary to obtain the volume fraction numerical scheme.

To obtain the local equations of each pure fluid k, we multiply the Euler equations (46) by the phase function χ_k of each fluid. This one only admits two values: $\chi_k(M,t)=1$ if the point M is located in the phase k at time t and $\chi_k(M,t)=0$ otherwise. This function obeys the local evolution equation:

$$\frac{\partial \chi_k}{\partial t} + \sigma_x \frac{\partial \chi_k}{\partial x} + \sigma_y \frac{\partial \chi_k}{\partial y} = 0, \tag{47}$$

where σ_x and σ_y are the components of the local interface velocity.

After some algebraic manipulations, the local pure fluids equations are given by:

$$\frac{\partial \chi_k U}{\partial t} + \frac{\partial \chi_k F}{\partial x} + \frac{\partial \chi_k G}{\partial y} = F^{\text{lag}} \frac{\partial \chi_k}{\partial x} + G^{\text{lag}} \frac{\partial \chi_k}{\partial y}, \tag{48}$$

where the Lagrangian fluxes are defined as $F^{\text{lag}} = F - \sigma_x U$ and $G^{\text{lag}} = G - \sigma_y U$.

For interface problems between pure inert fluids we have $\sigma_x = u$ and $\sigma_y = v$. In this case, the Lagrangian fluxes write $F^{\text{lag}} = [-u, 0, P, 0, Pu]^{\text{T}}$ and $G^{\text{lag}} = [-v, 0, 0, P, Pv]^{\text{T}}$.

Next we integrate in time and space over each computational cell $C_{i,j} =]x_{i-1/2}, x_{i+1/2}[\times]y_{j-1/2}, y_{j+1/2}[$ the Eq. (48):

$$\int_0^{\Delta t} \int_{C_{i,j}} \left(\frac{\partial \chi_k U}{\partial t} + \frac{\partial \chi_k F}{\partial x} + \frac{\partial \chi_k G}{\partial y} \right) \mathrm{d}V \, \mathrm{d}t = \int_0^{\Delta t} \int_{C_{i,j}} \left(F^{\text{lag}} \frac{\partial \chi_k}{\partial x} + G^{\text{lag}} \frac{\partial \chi_k}{\partial y} \right) \mathrm{d}V \, \mathrm{d}t. \tag{49}$$

Relation (49) can be written as:

$$I_1 + I_2 + I_2' = I_3 + I_3', \tag{50}$$

with

$$I_1 = \int_0^{\Delta t} \int_{C_{i,j}} \frac{\partial \chi_k U}{\partial t} \, \mathrm{d}V \, \mathrm{d}t,$$

$$I_2 = \int_0^{\Delta t} \int_{C_{i,j}} \frac{\partial \chi_k F}{\partial x} \, \mathrm{d}V \, \mathrm{d}t, \quad I_2' = \int_0^{\Delta t} \int_{C_{i,j}} \frac{\partial \chi_k G}{\partial y} \, \mathrm{d}V \, \mathrm{d}t,$$

$$I_3 = \int_0^{\Delta t} \int_{C_{i,j}} F^{\text{lag}} \frac{\partial \chi_k}{\partial x} \, \mathrm{d}V \, \mathrm{d}t, \quad I_3' = \int_0^{\Delta t} \int_{C_{i,j}} G^{\text{lag}} \frac{\partial \chi_k}{\partial y} \, \mathrm{d}V \, \mathrm{d}t.$$

Now these five integrals have to be determined to obtain the discrete macroscopic equations of each fluid. As an interface is not solved as a true discontinuity but rather as a diffusion zone (because of artificial smearing), it corresponds to a series of cells with various levels (volume fractions) of fluids, as shown in Fig. 13. In this way, at each cell boundary, we define a contact surface between fluids. For example, $S_{12,i-1/2}$ represents the contact surface at cell boundary $i - 1/2$ between fluid 1 on the left (present inside the cell $C_{i-1,j}$) and fluid 2 on the right (present inside the cell $C_{i,j}$). At each cell boundary, only four types of contact between pure fluids are possible. Each type of contact is associated to the corresponding surface.

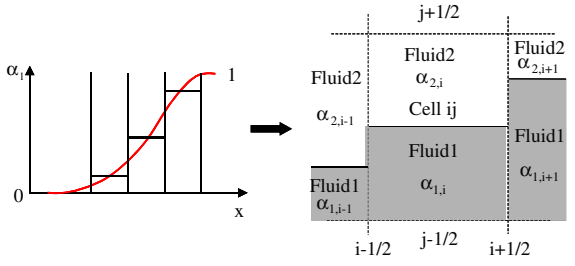

Fig. 13. Numerical representation of an interface in the discrete equations method.

Let us denote by (l,m) the configuration where the fluid l is present on the left and the fluid m is present on the right at a given cell boundary. At each contact (l,m), the corresponding Riemann problem is solved. Its solution, denoted in the following by the superscript '*', is used for the computation of the various fluxes (Eulerian and Lagrangian) that are then averaged over the cell surface.

In order to compute the integrals in (50), we define the following averaging operators:

- Volume average: $\langle f \rangle = \frac{1}{V_{ij}} \int_{V_{ij}} f \, \mathrm{d}V$.
- Surface averages: $\widehat{f} = \frac{1}{\Delta x} \int_{x_{i-1/2}}^{x_{i+1/2}} f \, \mathrm{d}x, \bar{f} = \frac{1}{\Delta y} \int_{y_{j-1/2}}^{y_{j+1/2}} f \, \mathrm{d}y$.
- Time average: $\widetilde{f} = \frac{1}{\Delta t} \int_0^{\Delta t} f \, \mathrm{d}t$.

4.1.1. Integration of the temporal term I_1

The first integral I_1 reads:

$$I_1 = \int_0^{\Delta t} \int_{C_{ij}} \frac{\partial \chi_k U}{\partial t} \, \mathrm{d}V \, \mathrm{d}t = \int_{C_{ij}} (\chi_k U)^{n+1} \, \mathrm{d}V - \int_{C_{ij}} (\chi_k U)^n \, \mathrm{d}V = \Big(\langle \chi_k U \rangle_{ij}^{n+1} - \langle \chi_k U \rangle_{ij}^n \Big) V_{ij}.$$

Using the volume average of the phase function χ_k in the cell C_{ij}, we have:

$$\langle \chi_k \rangle_{ij} = \frac{1}{V_{ij}} \int_{C_{ij}} \chi_k \, \mathrm{d}V = \frac{V_{k,ij}}{V_{ij}} \stackrel{\text{def}}{=} \alpha_{k,ij},$$

where $V_{k,ij}$ represents the volume occupied by the phase k in the cell C_{ij}.

Then, the term I_1 writes:

$$I_1 = \Big((\alpha_k \{U_k\})_{ij}^{n+1} - (\alpha_k \{U_k\})_{ij}^n \Big) V_{ij},$$

where $\{U_k\}_{ij} \stackrel{\text{def}}{=} \frac{1}{V_{k,ij}} \int_{C_{k,ij}} U_k \, \mathrm{d}V$ is the volume average of U_k in $V_{k,ij}$.

4.1.2. Integration of the convective fluxes I_2 and I_2'

The second integral I_2 reads:

$$I_2 = \int_0^{\Delta t} \int_{C_{ij}} \frac{\partial \chi_k F}{\partial x} \, \mathrm{d}V \, \mathrm{d}t = \int_0^{\Delta t} \int_{y_{j-1/2}}^{y_{j+1/2}} (\chi_k F)_{i+1/2} \, \mathrm{d}y \, \mathrm{d}t - \int_0^{\Delta t} \int_{y_{j-1/2}}^{y_{j+1/2}} (\chi_k F)_{i-1/2} \, \mathrm{d}y \, \mathrm{d}t.$$

Using the previous averages, we obtain:

$$I_2 = \Delta y \int_0^{\Delta t} (\overline{\chi_k F})_{i+1/2} \, \mathrm{d}t - \Delta y \int_0^{\Delta t} (\overline{\chi_k F})_{i-1/2} \, \mathrm{d}t = \Delta t \Delta y \Big((\widetilde{\overline{\chi_k F}})_{i+1/2} - (\widetilde{\overline{\chi_k F}})_{i-1/2} \Big).$$

In order to determine the average Eulerian flux $\widetilde{\chi_k F}$ at each cell boundary, we first compute the following surface averages:

$$\int_{y_{j-1/2}}^{y_{j+1/2}} (\chi_k F)_{i \pm 1/2} \, \mathrm{d}y = \sum_{l,m} \left(S \chi_k^* F^* \right)_{lm, i \pm 1/2},$$

where S_{lm} represents the contact surface for each pair of fluids in contact. Their expressions, reported in Table 1 for cell boundary $i - 1/2$, are obtained following simple arguments provided in [29]. $\chi_{k,lm}^*$ represents the phase function of fluid k for the same pair. Its value is reported in the same table and is obtained from the Riemann problem solution, according to the location of fluid k.

When fluid k is present on both sides of the interface, $\chi_k^* = 1$. When the other fluid is present on both sides, $\chi_k^* = 0$. These situations correspond to the first and last lines of Table 1, respectively.

Table 1
The different configurations for Eulerian fluxes at cell boundary $i-1/2$ for fluid $k=1$

Contact	Surface	Eulerian flux	Phase function χ_1^*
1–1	$S_{11}=\Delta y\,\min(\alpha_{1,i-1},\alpha_{1,i})$	F_{11}^*	$\chi_{1,11}^*=1$
1–2	$S_{12}=\Delta y\,\max(0,\alpha_{1,i-1}-\alpha_{1,i})$	F_{12}^*	$\chi_{1,12}^*=\begin{cases}1 & \text{if } u_{12}^*>0\\ 0 & \text{otherwise}\end{cases}$
2–1	$S_{21}=\Delta y\,\max(0,\alpha_{1,i}-\alpha_{1,i-1})$	F_{21}^*	$\chi_{1,21}^*=\begin{cases}1 & \text{if } u_{21}^*<0\\ 0 & \text{otherwise}\end{cases}$
2–2	$S_{22}=\Delta y\,\min(\alpha_{2,i-1},\alpha_{2,i})$	F_{22}^*	$\chi_{1,22}^*=0$

When fluid k is present on the left, $\chi_k^*=1$ only if the fluid k is entering the cell (line 2 of Table 1). When it is present on the right, $\chi_k^*=1$ only if the fluid k is leaving the cell (line 3 of Table 1).

As the Riemann problem is solved to determine the speed of the contact discontinuity u_{lm}^*, the whole solution is sampled along the axis $x/t=0$ and allows the various fluxes computation F_{lm}^*.

The Eulerian fluxes are supposed to be constant during a time step (CFL condition), thus we have:

$$I_2=\Delta t\left(\sum_{l,m}\left(S\chi_k^*F^*\right)_{lm,i+1/2}-\sum_{l,m}\left(S\chi_k^*F^*\right)_{lm,i-1/2}\right).$$

The third integral I_2' is obtained as previously:

$$I_2'=\int_0^{\Delta t}\int_{C_{ij}}\frac{\partial\chi_k G}{\partial y}\,\mathrm{d}t\,\mathrm{d}t=\Delta t\Delta x\left(\widetilde{(\chi_k G)}_{j+1/2}-\widetilde{(\chi_k G)}_{j-1/2}\right).$$

The Eulerian flux is obtained again by summing the different configurations of pairs in contact. Then, the integral I_2' reads:

$$I_2'=\Delta t\left(\sum_{l,m}\left(S\chi_k^*G^*\right)_{lm,j+1/2}-\sum_{l,m}\left(S\chi_k^*G^*\right)_{lm,j-1/2}\right).$$

4.1.3. Integration of the non-conservative terms I_3 and I_3'

The fourth integral I_3 provides the Lagrangian fluxes. It reads:

$$I_3=\int_0^{\Delta t}\int_{C_{ij}}F^{\mathrm{lag}}\frac{\partial\chi_k}{\partial x}\,\mathrm{d}V\,\mathrm{d}t=\int_0^{\Delta t}\int_{y_{j-1/2}}^{y_{j+1/2}}\int_{x_{i-1/2}}^{x_{i+1/2}}F^{\mathrm{lag}}\frac{\partial\chi_k}{\partial x}\,\mathrm{d}x\,\mathrm{d}y\,\mathrm{d}t.$$

The only interfaces present in the flow topology considered in Fig. 13 are located at the cell boundaries. Then, I_3 writes:

$$I_3=\int_0^{\Delta t}\int_{y_{j-1/2}}^{y_{j+1/2}}\left(F^{\mathrm{lag}}\left[\chi_k^x\right]\right)_{i-1/2}\mathrm{d}y\,\mathrm{d}t+\int_0^{\Delta t}\int_{y_{j-1/2}}^{y_{j+1/2}}\left(F^{\mathrm{lag}}\left[\chi_k^x\right]\right)_{i+1/2}\mathrm{d}y\,\mathrm{d}t,$$

where $\left[\chi_k^x\right]$ represents the jump of χ_k in the x-direction through an interface. As explained in [2], the preceding integration is allowed because the Lagrangian flux F^{lag} is uniform at every location where $\partial\chi_k/\partial x$ is non-zero.

By using the definitions of averages, we obtain:

$$I_3=\Delta t\Delta y\left(\widetilde{(\overline{F^{\mathrm{lag}}[\chi_k^x]})}_{i-1/2}+\widetilde{(\overline{F^{\mathrm{lag}}[\chi_k^x]})}_{i+1/2}\right).$$

Table 2
The different configurations for Lagrangian fluxes at cell boundary $i-1/2$ for fluid $k=1$

Contact	Surface	Lagrangian flux	Jump $[\chi_1^x]^*$
1–1	S_{11}	$F_{11}^{\mathrm{lag},*}$	$[\chi_1^x]^*_{11}=0$
1–2	S_{12}	$F_{12}^{\mathrm{lag},*}$	$[\chi_1^x]^*_{12}=\begin{cases}-1 & \text{if } u_{12}^*>0\\ 0 & \text{otherwise}\end{cases}$
2–1	S_{21}	$F_{21}^{\mathrm{lag},*}$	$[\chi_1^x]^*_{21}=\begin{cases}1 & \text{if } u_{21}^*>0\\ 0 & \text{otherwise}\end{cases}$
2–2	S_{22}	$F_{22}^{\mathrm{lag},*}$	$[\chi_1^x]^*_{22}=0$

As for the calculations of the Eulerian fluxes, we use the considerations described in Table 2 (for cell boundary $i-1/2$). By summing the different terms, we obtain:

$$\int_{y_{j-1/2}}^{y_{j+1/2}} \left(F^{\mathrm{lag}}[\chi_k^x]\right)_{i-1/2}\,\mathrm{d}y=\sum_{l,m}\left(SF^{\mathrm{lag},*}[\chi_k^{x,*}]\right)_{lm,i-1/2}.$$

The jump of the phase function is zero when the same fluid is present on both sides of the interface (lines 1 and 4 of Table 2). When the fluid under interest lies initially on the left and is entering the cell (line 2 of Table 2), the jump of its associated phase function is -1. When the fluid under interest lies on the right and the other fluid is entering the cell (line 3 of Table 2), the jump of its phase function is 1. The Lagrangian fluxes, in each type of contact, involve only the corresponding interface velocity and pressure that are provided by the Riemann solver.

For cell boundary $i+1/2$, we also have:

$$\int_{y_{j-1/2}}^{y_{j+1/2}} \left(F^{\mathrm{lag}}[\chi_k^x]\right)_{i+1/2}\,\mathrm{d}y=\sum_{l,m}\left(SF^{\mathrm{lag},*}[\chi_k^{x,*}]\right)_{lm,i+1/2}.$$

Assuming the Lagrangian fluxes are constant during the time step, we have:

$$I_3=\Delta t\left(\sum_{l,m}\left(SF^{\mathrm{lag},*}[\chi_k^{x,*}]\right)_{lm,i-1/2}+\sum_{l,m}\left(SF^{\mathrm{lag},*}[\chi_k^{x,*}]\right)_{lm,i+1/2}\right).$$

The last integral I_3' is obtained similarly:

$$I_3'=\int_0^{\Delta t}\int_{C_{ij}} G^{\mathrm{lag}}\frac{\partial\chi_k}{\partial y}\,\mathrm{d}V\,\mathrm{d}t=\Delta t\Delta x\left(\widetilde{(G^{\mathrm{lag}}[\chi_k^y])}_{j-1/2}+\widetilde{(G^{\mathrm{lag}}[\chi_k^y])}_{j+1/2}\right)$$

and

$$I_3'=\Delta t\left(\sum_{l,m}\left(SG^{\mathrm{lag},*}[\chi_k^{y,*}]\right)_{lm,j-1/2}+\sum_{l,m}\left(SG^{\mathrm{lag},*}[\chi_k^{y,*}]\right)_{lm,j+1/2}\right).$$

Finally, the numerical scheme (50) reads, for each fluid k:

$$\begin{aligned}&\frac{(\alpha_k\{U_k\})_{ij}^{n+1}-(\alpha_k\{U_k\})_{ij}^{n}}{\Delta t}+\frac{\widetilde{(\chi_k F)}_{i+1/2}-\widetilde{(\chi_k F)}_{i-1/2}}{\Delta x}+\frac{\widetilde{(\chi_k G)}_{j+1/2}-\widetilde{(\chi_k G)}_{j-1/2}}{\Delta y}\\&\quad=\frac{\widetilde{(F^{\mathrm{lag}}[\chi_k^x])}_{i-1/2}+\widetilde{(F^{\mathrm{lag}}[\chi_k^x])}_{i+1/2}}{\Delta x}+\frac{\widetilde{(G^{\mathrm{lag}}[\chi_k^y])}_{j-1/2}+\widetilde{(G^{\mathrm{lag}}[\chi_k^y])}_{j+1/2}}{\Delta y},\end{aligned}\tag{51}$$

where all terms have been divided by $\Delta x\Delta y\Delta t$ and with

$$(\widetilde{\overline{\chi_k F}})_{i\pm1/2} = \frac{1}{\Delta y}\sum_{l,m}\left(S\chi_k^* F^*\right)_{lm,i\pm1/2}, \quad (\widetilde{\overline{\chi_k G}})_{j\pm1/2} = \frac{1}{\Delta x}\sum_{l,m}\left(S\chi_k^* G^*\right)_{lm,j\pm1/2},$$

$$(\widetilde{\overline{F^{\mathrm{lag}}[\chi_k^x]}})_{i\pm1/2} = \frac{1}{\Delta y}\sum_{l,m}\left(SF^{\mathrm{lag},*}[\chi_k^{x,*}]\right)_{lm,i\pm1/2}, \quad (\widetilde{\overline{G^{\mathrm{lag}}[\chi_k^y]}})_{j\pm1/2} = \frac{1}{\Delta x}\sum_{l,m}\left(SG^{\mathrm{lag},*}[\chi_k^{y,*}]\right)_{lm,j\pm1/2}.$$

4.2. Implementation of the reactive Riemann solver into the DEM

In Fig. 4, we have represented an example of waves pattern in a (x,t) diagram representing the solution of the reactive Riemann problem associated to an evaporation front. An additional wave appears compared to the non-reactive case: the evaporation front. This one is a discontinuity separating the superheated liquid and its pure vapor when the evaporation process is total, and a liquid–vapor mixture in thermodynamic equilibrium when the evaporation is partial. The front appearance comes from the fact that the liquid becomes superheated ($P_l < P_{\mathrm{sat}}(T_l)$). Moreover, the presence or absence of the mixture behind the front is determined in accordance to the location of the CJ deflagration point in the (P,v) diagram. If $\rho_{CJ} < \rho_{g,\mathrm{sat}}(T_{CJ})$, the evaporation is total (CJ state outside the saturation dome). Otherwise, the evaporation is partial (CJ state inside the saturation dome).

In addition, such a front obeys the Rankine–Hugoniot relations $[F - \sigma U] = 0$ (σ is the front velocity), where F and U indicate, respectively, the flux and the conservative variables vector of pure fluid Euler equations in the total evaporation case or homogeneous Euler equations in the partial evaporation case.

Thus two fundamental ingredients are available:

- the evaporation front is the location where the phase functions have jumps,
- the front obeys the Rankine–Hugoniot relations $[F - \sigma U] = 0$.

Indeed, the dynamic vapor appearance behind the front creates a jump of its phase function. Then a jump of the liquid phase function is created which is opposite to the vapor one. The same situation occurs when a liquid–vapor mixture appears behind the front taking into account that part of the liquid determined by the reactive Riemann solver does not change into vapor.

The terms $F - \sigma U$ associated to evaporation fronts, named reactive fluxes, have the same purpose as the Lagrangian fluxes corresponding to the particular case $\sigma = u$. These reactive fluxes are constant across phase functions discontinuities.

It is also important to note that the dynamic vapor appearance behind the front will modify the jumps of the phase functions across the contact discontinuity as represented in Fig. 14.

Indeed, in the inert case, the evaporation front is absent and only the fluids initially present are recovered on both sides of the contact discontinuity. In the reactive case, vapor appears at the contact discontinuity. Then the Lagrangian fluxes are modified as well as the jumps of the phase functions, as shown in Fig. 14.

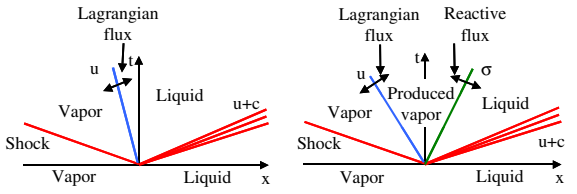

Fig. 14. Resolution of the inert (left) and the reactive (right) Riemann problem.

When the evaporation is total, the jumps are zero at the contact discontinuity for the situation depicted on this figure. When the evaporation is partial, the situation is more complicated and is detailed in Appendix B. The same type of remarks holds at the front level. For the sake of clarity, we only consider in the following total evaporation fronts. The implementation of partial evaporation fronts is described in Appendix B.

For a better understanding, we adopt some notations indicating if the resolution of a Riemann problem is inert or reactive. The Riemann problem solution corresponds to the inert one when the liquid is not superheated, i.e., if the 'reactivity' test ($P^* < P_{sat}(T^*)$) is not fulfilled. The different fluxes and the associated phase functions will be given in accordance with these notations, described in Table 3.

In addition, in the particular Riemann problem (1–1), two evaporation fronts may appear. They will be denoted by the subscripts l and r when they are facing, respectively, to the left and to the right.

We now consider the integrals of Eq. (50) that must be determined in the reactive case.

The temporal term I_1 remains unchanged while the convective fluxes I_2 and I'_2 and the non-conservative terms I_3 and I'_3 have to be modified.

4.2.1. Integration of the convective fluxes I_2 and I'_2

The dynamic vapor appearance changes the values of the phase function χ_k^*. For example, the solution of the reactive Riemann problem represented in Fig. 14 indicates that vapor is present at $x/t = 0$ while the associated inert solution leads to the presence of liquid.

Assuming fluid 1 is a liquid and fluid 2 is its associated vapor, the values of χ_1^* in Table 1 must be modified when the Riemann problems are reactive. Then, the sampling at $x/t = 0$ is done with respect to u^* (contact discontinuity velocity) and σ^* (front velocity) as represented in Table 4.

When vapor is present initially on both sides of the contact (last line of Table 4), the phase function of fluid 1 is necessary 0.

When fluid 1 is present on one side only, two instances have to be considered. This fluid may remain liquid, the inert Riemann problem thus provides the same solution regarding χ_1^* and F^* as in Table 1 (lines 5 and 7 of Table 4). When fluid 1 becomes superheated, vapor is produced behind the front.

Thus, when fluid 1 is initially on the left and the front is entering the cell, $\chi_1^* = 1$ (line 6 of Table 4). Such instance occurs when the liquid velocity is positive and larger than the front velocity that faces to left. Symmetrically, when fluid 1 is initially on the right and the front is leaving the cell, $\chi_1^* = 1$ (line 8 of Table 4). Such case occurs when the liquid velocity is negative and larger than the front velocity that faces to right. The first line of Table 4 corresponds to the case with two inert liquids in contact already examined in Table 1. The three next cases are more complex.

We consider first the case where only the liquid on the left is superheated (line 2 of Table 4) corresponding to a reactive front facing to left $(R)_l$. In this case, the contact discontinuity separates vapor produced behind the front on the left and inert liquid on the right. When the front velocity is negative and the velocity of the contact discontinuity is positive, then only vapor is present along the $x/t = 0$ axis. Otherwise, fluid 1 crosses the cell boundary.

The third line of Table 4 summarizes the symmetric instance (evaporation front facing to right). The fourth line of Table 4 summarizes the instance of two reactive fronts facing, respectively, to left and right producing both pure vapor.

Table 3
Notations associated with the resolution of Riemann problems

Notations	Significations
(R)	Reactive Riemann problem
(I)	Inert Riemann problem

Table 4
The different configurations for Eulerian fluxes at cell boundary $i-1/2$ for fluid $k=1$ in the presence of total evaporation fronts

Contact	Surface	Eulerian flux	Type	Phase function χ_1^*
1–1	S_{11}	F_{11}^*	(I)	$\chi_{1,11}^* = 1$
			$(R)_\mathrm{l}$	$\chi_{1,11}^* = \begin{cases} 0 & \text{if } \sigma_{11,\mathrm{l}}^* < 0 < u_{11}^* \\ 1 & \text{otherwise} \end{cases}$
			$(R)_\mathrm{r}$	$\chi_{1,11}^* = \begin{cases} 0 & \text{if } u_{11}^* < 0 < \sigma_{11,\mathrm{r}}^* \\ 1 & \text{otherwise} \end{cases}$
			$(R)_\mathrm{l}$ $(R)_\mathrm{r}$	$\chi_{1,11}^* = \begin{cases} 0 & \text{if } \sigma_{11,\mathrm{l}}^* < 0 < \sigma_{11,\mathrm{r}}^* \\ 1 & \text{otherwise} \end{cases}$
1–2	S_{12}	F_{12}^*	(I)	$\chi_{1,12}^* = \begin{cases} 1 & \text{if } u_{12}^* > 0 \\ 0 & \text{otherwise} \end{cases}$
			(R)	$\chi_{1,12}^* = \begin{cases} 1 & \text{if } \sigma_{12}^* > 0 \\ 0 & \text{otherwise} \end{cases}$
2–1	S_{21}	F_{21}^*	(I)	$\chi_{1,21}^* = \begin{cases} 1 & \text{if } u_{21}^* < 0 \\ 0 & \text{otherwise} \end{cases}$
			(R)	$\chi_{1,21}^* = \begin{cases} 1 & \text{if } \sigma_{21}^* < 0 \\ 0 & \text{otherwise} \end{cases}$
2–2	S_{22}	F_{22}^*	(I)	$\chi_{1,22}^* = 0$

Taking into account all instances summarized in Table 4, the formulas of the convective fluxes remain unchanged:

$$I_2 = \Delta t \Delta y \left((\widetilde{\chi_k F})_{i+1/2} - (\widetilde{\chi_k F})_{i-1/2} \right) = \Delta t \left(\sum_{l,m} \left(S \chi_k^* F^* \right)_{lm,i+1/2} - \sum_{l,m} \left(S \chi_k^* F^* \right)_{lm,i-1/2} \right),$$

$$I_2' = \Delta t \Delta x \left((\widetilde{\chi_k G})_{j+1/2} - (\widetilde{\chi_k G})_{j-1/2} \right) = \Delta t \left(\sum_{l,m} \left(S \chi_k^* G^* \right)_{lm,j+1/2} - \sum_{l,m} \left(S \chi_k^* G^* \right)_{lm,j-1/2} \right).$$

4.2.2. Integration of the non-conservative terms I_3 and I_3'

Contrary to convective fluxes, the integration of the terms $\int_{y_{j-1/2}}^{y_{j+1/2}} (F - \sigma U)[\chi_k^x] \, \mathrm{d}y$ on each cell boundary leads to additional terms named reactive fluxes.

For each reactive Riemann problem (see Fig. 15), this integral may be splitted in two types of terms. The first one comes from the contact discontinuity (Lagrangian fluxes) and the second one is associated to the presence of the reactive front (reactive fluxes):

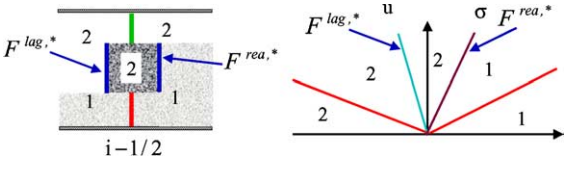

Fig. 15. Lagrangian and reactive fluxes in the Riemann problem (2−1) for a total evaporation front.

$$\int_{y_{j-1/2}}^{y_{j+1/2}} (F - \sigma U)\left[\chi_k^x\right] \mathrm{d}y = \sum_{l,m} S_{lm}\left(F^{\mathrm{lag},*}\left[\chi_k^x\right]^* + F^{\mathrm{rea},*}\left[\chi_k^x\right]^*\right)_{lm}.$$

Integrations are possible because the Lagrangian and the transfer fluxes are uniform across contact discontinuities and reactive fronts, respectively:

$$F^{\mathrm{lag}} = [-u,\ 0,\ P,\ 0,\ Pu]^{\mathrm{T}}, \quad F^{\mathrm{rea}} = [-\sigma,\ m,\ mu + P,\ muv,\ mE + Pu]^{\mathrm{T}},$$

where $m = \rho(u - \sigma)$ is the mass flow rate across the reactive front.

The Lagrangian fluxes and the associated jumps of the phase function χ_1 across the contact discontinuities are summarized in Table 5 for cell boundary $i - 1/2$.

We detail the first type of contact (1–1) that is the most complicated. The first line of Table 5 corresponds to the absence of reactive fronts. Fluid 1 remaining present on both sides of the contact discontinuity, the jump of its phase function is necessarily zero. Similarly, when two fronts are present (line 4 of Table 5) there is no jump of the phase function since vapor is present on both sides of the contact discontinuity.

We now consider presence of superheated liquid only on the left (line 2 of Table 5). When the velocity of the contact discontinuity, separating the produced vapor on the left and the inert liquid on the right, is negative, no jump of the phase function is present inside the cell. Otherwise, this jump is necessarily 1.

Symmetrically, when the superheated liquid lies on the right only (line 3 of Table 5) and the velocity of the contact discontinuity is positive, the jump is -1 since the produced vapor is on the right and the inert liquid is on the left. The other instances of Table 5 follow the same logic.

When reactive Riemann problems are considered, we can notice that the jump of the phase functions are zero in most cases, contrarily to the inert case (see Table 2). Thus most interactions between fluids (liquid

Table 5
The different configurations for Lagrangian fluxes at cell boundary $i - 1/2$ for fluid $k = 1$ in the presence of total evaporation fronts

Contact	Surface	Lagrangian flux	Type	Jump $\left[\chi_1^x\right]^*$
1–1	S_{11}	$F_{11}^{\mathrm{lag},*}$	(I)	$[\chi_1^x]_{11}^* = 0$
			$(R)_{\mathrm{l}}$	$[\chi_1^x]_{11}^* = \begin{cases} 1 & \text{if } u_{11}^* > 0 \\ 0 & \text{otherwise} \end{cases}$
			$(R)_{\mathrm{r}}$	$[\chi_1^x]_{11}^* = \begin{cases} -1 & \text{if} \mid u_{11}^* > 0 \\ 0 & \text{otherwise} \end{cases}$
			$(R)_{\mathrm{l}}$ $(R)_{\mathrm{r}}$	$[\chi_1^x]_{11}^* = 0$
1–2	S_{12}	$F_{12}^{\mathrm{lag},*}$	(I)	$[\chi_1^x]_{12}^* = \begin{cases} -1 & \text{if } u_{12}^* > 0 \\ 0 & \text{otherwise} \end{cases}$
			(R)	$[\chi_1^x]_{12}^* = 0$
2–1	S_{21}	$F_{21}^{\mathrm{lag},*}$	(I)	$[\chi_1^x]_{21}^* = \begin{cases} 1 & \text{if } u_{21}^* > 0 \\ 0 & \text{otherwise} \end{cases}$
			(R)	$[\chi_1^x]_{21}^* = 0$
2–2	S_{22}	$F_{22}^{\mathrm{lag},*}$	(I)	$[\chi_1^x]_{22}^* = 0$

Table 6
The different configurations for reactive fluxes at cell boundary $i-1/2$ for fluid $k=1$ in the presence of total evaporation fronts

Contact	Surface	Type	Reactive flux	Jump $[\chi_1^x]^*$
1–1	S_{11}	$(R)_\mathrm{l}$	$F_{11,\mathrm{l}}^{\mathrm{rea},*}$	$[\chi_1^x]^*_{11,\mathrm{l}} = \begin{cases} -1 & \text{if } \sigma^*_{11,\mathrm{l}} > 0 \\ 0 & \text{otherwise} \end{cases}$
		$(R)_\mathrm{r}$	$F_{11,\mathrm{r}}^{\mathrm{rea},*}$	$[\chi_1^x]^*_{11,\mathrm{r}} = \begin{cases} 1 & \text{if } \sigma^*_{11,\mathrm{r}} > 0 \\ 0 & \text{otherwise} \end{cases}$
1–2	S_{12}	(R)	$F_{12}^{\mathrm{rea},*}$	$[\chi_1^x]^*_{12} = \begin{cases} -1 & \text{if } \sigma^*_{12} > 0 \\ 0 & \text{otherwise} \end{cases}$
2–1	S_{21}	(R)	$F_{21}^{\mathrm{rea},*}$	$[\chi_1^x]^*_{21} = \begin{cases} 1 & \text{if } \sigma^*_{21} > 0 \\ 0 & \text{otherwise} \end{cases}$

and vapor) are carried out from contact discontinuities to reactive fronts. The different configurations concerning these additional reactive fluxes are summarized in Table 6.

We detail the situations that appear when fluid 1 is initially on both sides of the contact. When a reactive front is present and faces to left (line 1 of Table 6), the jump of the phase function is -1 when the front velocity is positive. Otherwise, the jump is zero. Symmetrically, when a front faces to right (line 2 of Table 6), the jump is 1 when the front velocity is positive. The same conclusions provide the data of lines 3 and 4 of Table 6.

The large number of configurations mentioned previously in the different tables shows the complexity of the coupling between the reactive Riemann problem and the discrete equations method. According to the solutions provided by the resolution of the Riemann problem, additional terms appear and modify the terms present initially in the numerical scheme (51).

Then, the numerical scheme of the reactive discrete equations method (RDEM) reads for each fluid k:

$$\frac{(\alpha_k\{U_k\})_{ij}^{n+1} - (\alpha_k\{U_k\})_{ij}^{n}}{\Delta t} + \frac{(\widetilde{\overline{\chi_k F}})_{i+1/2} - (\widetilde{\overline{\chi_k F}})_{i-1/2}}{\Delta x} + \frac{(\widetilde{\widehat{\chi_k G}})_{j+1/2} - (\widetilde{\widehat{\chi_k G}})_{j-1/2}}{\Delta y}$$
$$= \begin{pmatrix} \frac{(\widetilde{\overline{F^{\mathrm{lag}}[\chi_k^x]}})_{i-1/2} + (\widetilde{\overline{F^{\mathrm{lag}}[\chi_k^x]}})_{i+1/2}}{\Delta x} + \frac{(\widetilde{\overline{F^{\mathrm{rea}}[\chi_k^x]}})_{i-1/2} + (\widetilde{\overline{F^{\mathrm{rea}}[\chi_k^x]}})_{i+1/2}}{\Delta x} \\ + \frac{(\widetilde{\widehat{G^{\mathrm{lag}}[\chi_k^y]}})_{j-1/2} + (\widetilde{\widehat{G^{\mathrm{lag}}[\chi_k^y]}})_{j+1/2}}{\Delta y} + \frac{(\widetilde{\widehat{G^{\mathrm{rea}}[\chi_k^y]}})_{j-1/2} + (\widetilde{\widehat{G^{\mathrm{rea}}[\chi_k^y]}})_{j+1/2}}{\Delta y}, \end{pmatrix} \tag{52}$$

where

$$(\widetilde{\overline{\chi_k F}})_{i\pm1/2} = \frac{1}{\Delta y}\sum_{l,m}\left(S\chi_k^* F^*\right)_{lm,i\pm1/2}, \qquad (\widetilde{\widehat{\chi_k G}})_{j\pm1/2} = \frac{1}{\Delta x}\sum_{l,m}\left(S\chi_k^* G^*\right)_{lm,j\pm1/2},$$

$$(\widetilde{\overline{F^{\mathrm{lag}}[\chi_k^x]}})_{i\pm1/2} = \frac{1}{\Delta y}\sum_{l,m}\left(SF^{\mathrm{lag},*}[\chi_k^{x,*}]\right)_{lm,i\pm1/2} \quad (\widetilde{\overline{F^{\mathrm{rea}}[\chi_k^x]}})_{i\pm1/2} = \frac{1}{\Delta y}\sum_{l,m}(SF^{\mathrm{rea},*}[\chi_k^{x,*}])_{lm,i\pm1/2},$$

$$(\widetilde{\widehat{G^{\mathrm{lag}}[\chi_k^y]}})_{j\pm1/2} = \frac{1}{\Delta x}\sum_{l,m}\left(SG^{\mathrm{lag},*}[\chi_k^{y,*}]\right)_{lm,j\pm1/2}, \quad (\widetilde{\widehat{G^{\mathrm{rea}}[\chi_k^y]}})_{j\pm1/2} = \frac{1}{\Delta x}\sum_{l,m}(SG^{\mathrm{rea},*}[\chi_k^{y,*}])_{lm,j\pm1/2}.$$

In the next section, we present numerical results obtained with this scheme and validations over experiments.

5. Numerical results

In this section, we provide one-dimensional validations of the reactive discrete equations method (RDEM) built in the previous section and two-dimensional illustrations.

5.1. One-dimensional validations

Two situations involving reactive fronts are examined. The first one concerns evaporation fronts. The results obtained with the reactive discrete equations method (RDEM) are compared to those obtained with the exact reactive Riemann solver. The second situation, involving detonation fronts, is also examined in order to illustrate the method capabilities. All these tests are realized with a mesh involving 1000 computational cells.

5.1.1. Evaporation front

In this simulation, the two phases correspond to liquid dodecane and its associated vapor whose EOS parameters are given in Section 2. The initial configuration, close to the experimental conditions given in [33], corresponds to the one described in Section 3 where an exact solution is provided in Fig. 11.

The numerical solution (symbols) and the exact solution (lines) are represented at time $t = 370$ μs in Fig. 16. The mixture density and the pressure are represented in logarithmic scales.

In this figure, we can observe an excellent agreement between the solutions. The jump relations across the reactive front are correctly computed by the non-conservative terms of the method. We can also notice that the method correctly handles the interface conditions across the contact discontinuity separating the

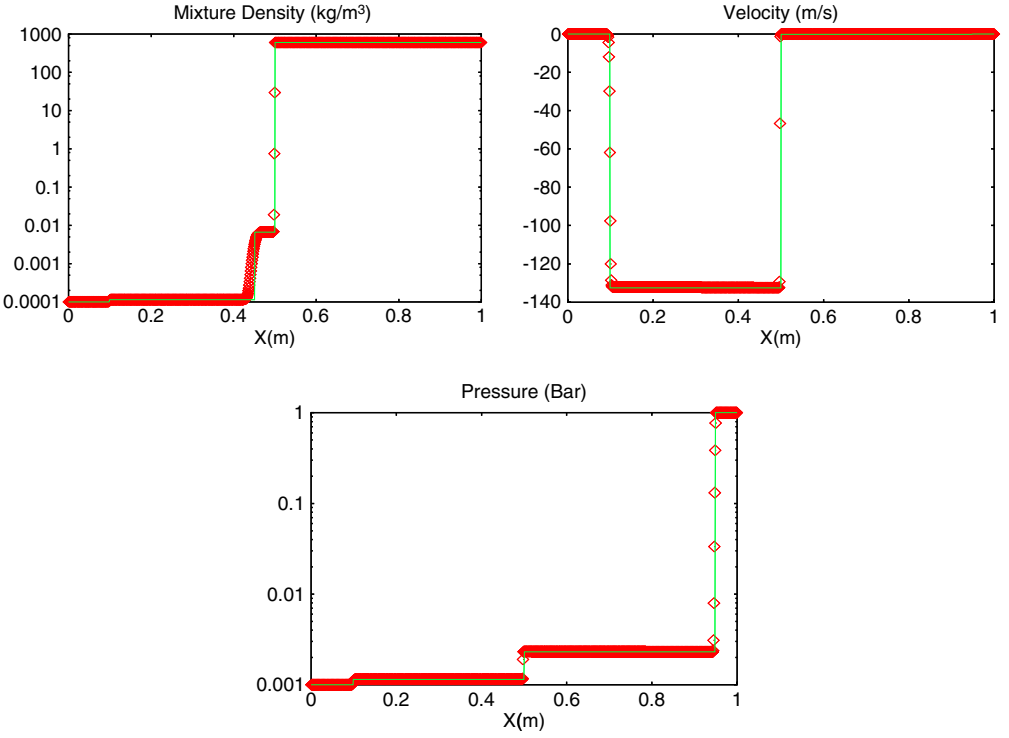

Fig. 16. Numerical (symbols) and exact (lines) solutions of the liquid–vapor expansion tube.

shocked and the produced vapor. The same remark holds for the isentrope connecting the initial state of the liquid with a metastable state, involving a pressure drop. As the density and consequently the sound speed remain nearly constant, the isentrope looks like a discontinuity, as represented in the pressure graph. Finally, we can note that the numerical diffusion associated to the front is negligible because the front speed is relatively low (0.6 m/s).

5.1.2. Propagation of a detonation front

To perform such computations, the RDEM described in the previous section does not need any modification. However, the Riemann solver necessitates the introduction of detonation fronts instead of deflagration waves. Such modifications are detailed in Appendix A.

We consider a condensed explosive and its gaseous products whose parameters are given in [13]. The explosive parameters are $\gamma = 3$, $P_\infty = 0$ Pa and $q = 4.5156 \times 10^6$ J/kg. Those of the products are $\gamma = 3$, $P_\infty = 0$ Pa and $q = 0$ J/kg.

Piston boundary conditions are used at the left side of a 1-m length domain filled with the explosive to simulate the impact of a projectile at the velocity of 1000 m/s.

In Fig. 17, numerical solutions are represented at times $t = 30$ μs, $t = 60$ μs, $t = 90$ μs and $t = 120$ μs, showing the propagation of the detonation front into the explosive. The horizontal lines represent the theoretical values of the CJ detonation state. On the numerical results curves, the slope change in the various profiles is characteristic of the CJ detonation point. It is clear that the CJ state is correctly computed as we can see in this figure.

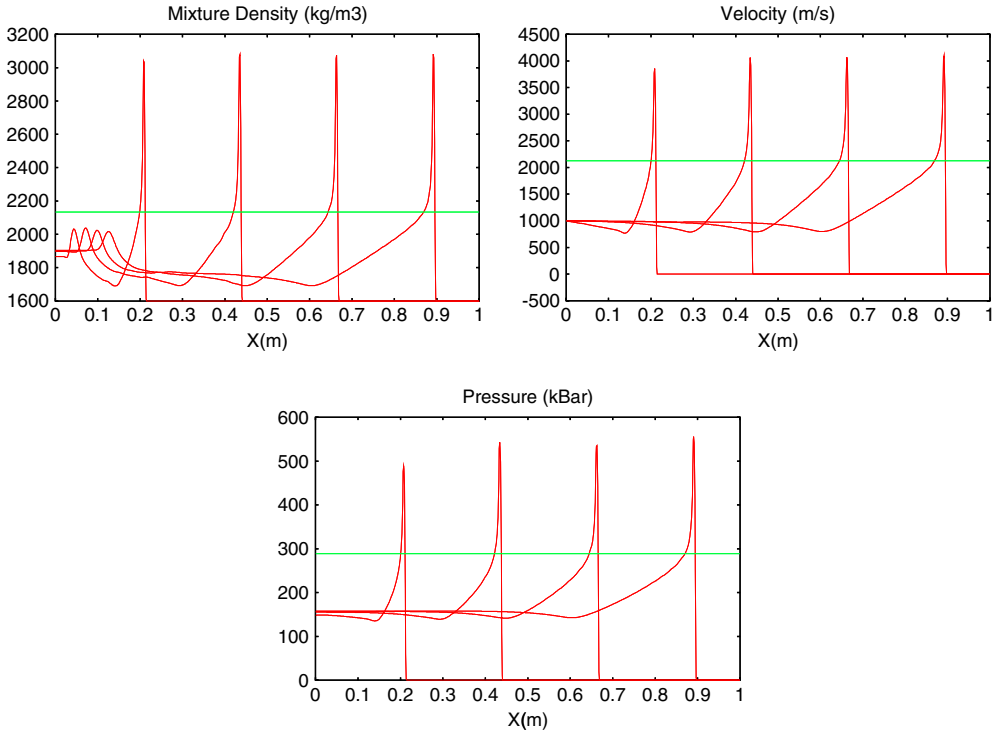

Fig. 17. Propagation of a detonation front into a condensed explosive. The horizontal lines represent the theoretical values of the CJ detonation point.

The present method contains two important features:

- the chemical decomposition rates of the condensed explosive, that are very difficult to determine from experiments, are not necessary,
- solving the reaction zone is useless.

The detonation dynamics is directly introduced in the reactive Riemann problem, built in Appendix A, by the way of the Rankine–Hugoniot relations and the CJ detonation relation. This last relation may also be replaced by more sophisticated kinetic relations such as those proposed by [6,7,40].

We shall see later that this method is able to propagate multi-dimensional detonation fronts.

5.2. Two-dimensional tests

The aim of this subsection is to illustrate the method capabilities concerning the multi-dimensional propagation of permeable fronts. As a limit situation, we first examine the case of a non-permeable interface by studying the interaction of a shock wave with a light gas bubble. We then examine subsonic front propagation in two evaporation test problems. The first consists in supercavitation over a high velocity underwater projectile. Computed results are compared with experiments. The second test consists in the computation of cavitation effects and dynamic appearance of interfaces in diesel injection nozzles. We then address supersonic fronts by considering the 2D dynamics of a detonation wave propagating into a condensed explosive and interacting with material interfaces.

5.2.1. Non-permeable fronts: shock–interface interaction

The initial configuration of this simulation is described in Fig. 18. It consists in the study of the interaction of an incident shock wave propagating into a heavy gas with a light gas bubble.

A high pressure chamber ($P = 5.6 \times 10^5$ Pa) filled with air at density $\rho = 3.92$ kg/m^3 is connected to a chamber filled with air at atmospheric pressure and normal density. In this chamber, a light gas bubble (helium) at density $\rho = 0.16$ kg/m^3 is present. The two fluids obey the ideal gas EOS with different polytropic coefficients.

The numerical results (900×360 computational cells) are shown in the right column of Fig. 19 as a Schlieren diagram of the mixture density. The results are represented at times $t = 202$ μs, $t = 396$ μs, $t = 596$ μs and $t = 797$ μs from up to down.

In addition, shock tube experiments with the initial configuration described in Fig. 18 have been done at POLYTECH Marseille, by the research group leaded by Pr.Houas. The associated experimental results (shadowgraphs) are represented at the left column of Fig. 19. The time interval between two successive _photographs is $\Delta t = 210$ μs.

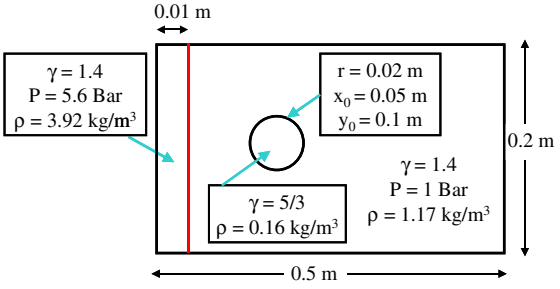

Fig. 18. Initial configuration of a shock tube with a light gas bubble.

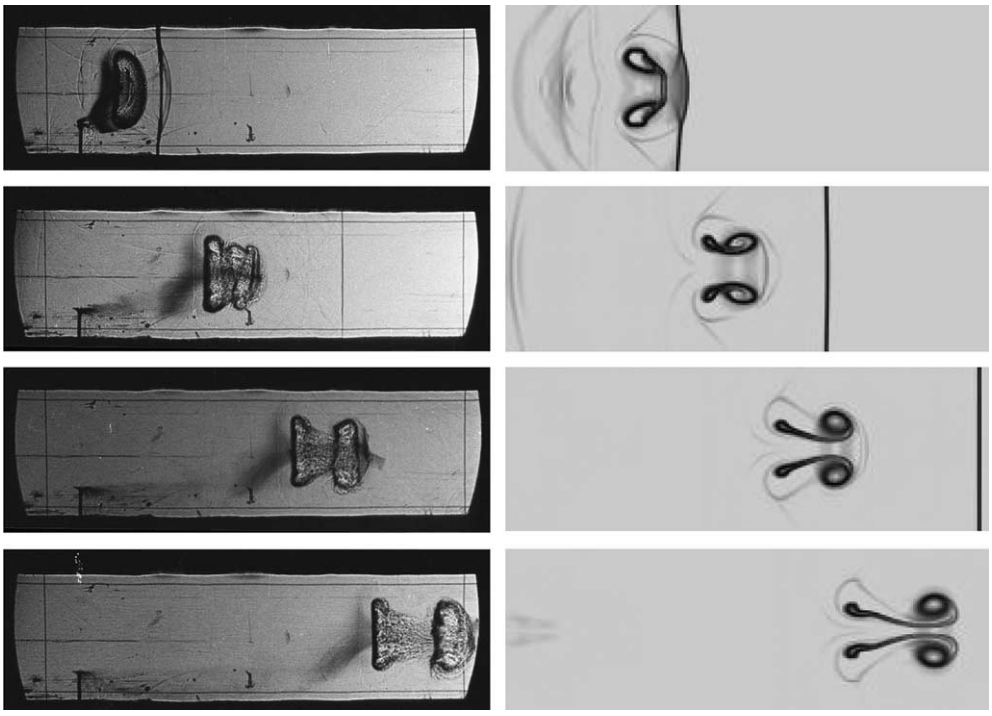

Fig. 19. Experimental (left) and numerical (right) results of a shock-bubble interaction. The experimental results (shadowgraphs) have been obtained by courtesy of Dr. Layes. The numerical results correspond to density gradient contours (dark areas show high density gradient levels).

We can first notice that experimental and numerical results are qualitatively similar. At atmospheric pressure, the sound speed in the light fluid ($c = 1020$ m/s) is much larger than the one in the air ($c = 346$ m/s). Thus the shock speed is higher inside the bubble than outside as we can observe in the first photographs (left and right). The shock is accelerated but recovers its original shape since the second pictures. The shock interaction with the interface produces a Richtmyer–Meshkov instability resulting in a high velocity heavy fluid jet that contracts the bubble and induces its rotation as we can see in the last views. It appears clearly that the method is able to solve contact/interface problems.

5.2.2. Subsonic evaporation fronts: supercavitation over obstacle

A solid high velocity projectile ($u = 650$ m/s) is launched from a gun into a tank filled with water. A flash X-ray radiograph allows the visualization of the cavitation pocket around the projectile. Such experimental facility has been built at ISL (French-German Institute of Saint-Louis). The measurements have been led by [31] and are shown in the top of Fig. 20.

We realize the numerical simulation of this experiment under the same conditions with the present method where the evaporation front is solved as a CJ deflagration wave. The projectile is treated as an obstacle at rest with an incoming liquid at the velocity $u = 650$ m/s. The water is initially at atmospheric pressure with density $\rho = 1000$ kg/m^3. The liquid and vapor thermodynamics is represented by a 'Stiffened Gas' EOS whose parameters are given in Section 2. The numerical result (mixture density contours) is shown in the bottom of Fig. 20. We can notice that the numerical and experimental results are qualitatively identical.

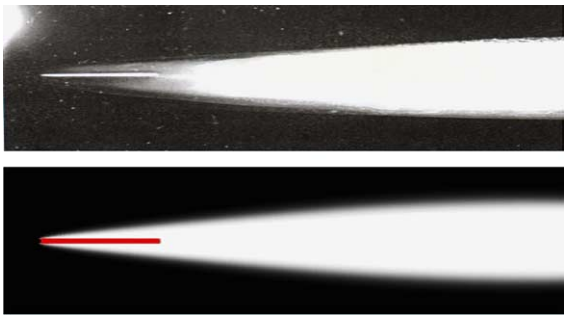

Fig. 20. Experimental (top) and numerical (bottom) results. The experimental result (radiograph) has been obtained by courtesy of Dr. Schaffar. The numerical result correspond to mixture density contours (pale areas show low density levels).

5.2.3. Subsonic evaporation fronts: cavitation in liquid fuel injectors

We consider a nozzle connected to a high pressure tank ($P = 10^8$ Pa) filled with liquid dodecane at density $\rho = 600$ kg/m^3. The nozzle outlet is connected to an engine combustion chamber where the pressure is of the order of 10^5 Pa. The large pressure ratio combined to the converging geometry of the nozzle produces a high velocity ($\simeq$200 m/s) liquid jet into the combustion chamber. The efficiency of the injection as well as atomization inside the combustion chamber strongly depends on cavitation effects occurring inside the nozzle [3,4]. The aim of this paragraph is to show that the present method is able to compute vapor creation and cavitation pockets in such device.

The initial configuration of the simulation (600×600 computational cells) is shown in Fig. 21. The thermodynamics parameters of liquid and vapor dodecane are the same as those used previously in the first one-dimensional test. A third fluid (air) at density $\rho = 1$ kg/m^3 is present initially inside the injection duct. Its associated EOS parameters are $\gamma = 1.4$ and $P_\infty = 0$ Pa.

The vapor volume fraction contours are shown in Fig. 22 at times $t = 2.5$ μs, $t = 73$ μs, $t = 143$ μs, $t = 230$ μs, $t = 323$ μs and $t = 422$ μs. The temporal evolution is done from up to down and left to right.

At the first instants, the high-pressure liquid is travelled by expansion waves because it is in contact with the low-pressure air. Effects similar to the one-dimensional expansion tube test represented in Fig. 16 are present. At the free surface an evaporation front appears and produces vapor dodecane. The vapor flows through the nozzle as well as the liquid. Cavitation pockets are created at the corner and the tip of the needle as shown in pictures 2 and 3. At the same time, a cavitation pocket appears at the nozzle throat. In the

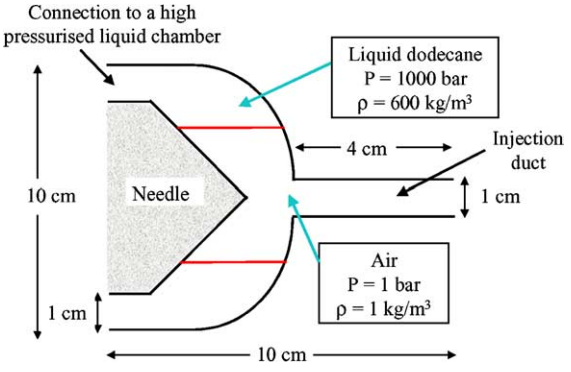

Fig. 21. Initial configuration of a high pressure fuel injector.

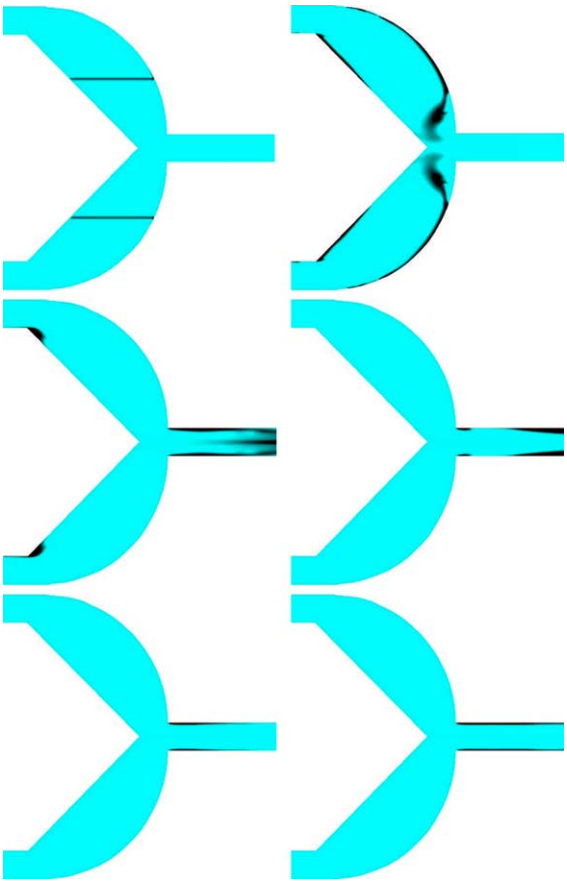

Fig. 22. Temporal evolution of the vapor volume fraction in a high pressure fuel injector (dark areas show high volume fraction levels).

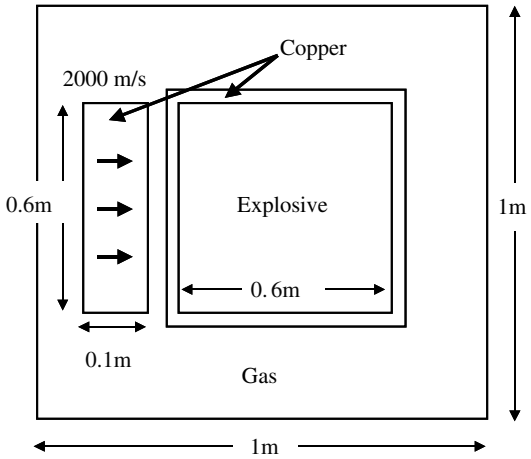

Fig. 23. Initial configuration of an impact over a tank filled with explosive.

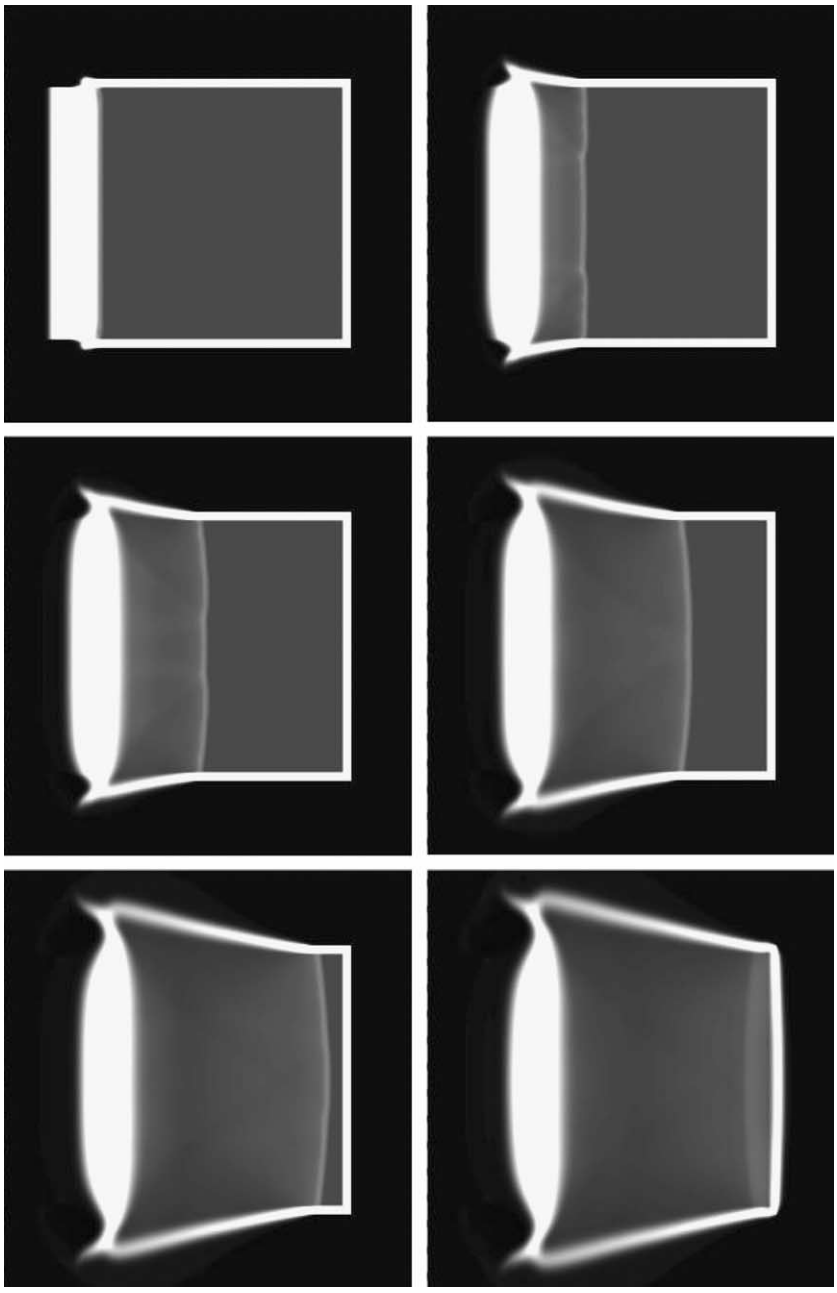

Fig. 24. Temporal evolution of the mixture density : two-dimensional propagation of a detonation front (pale areas show high density levels).

further pictures, the pocket settled at the corner of the needle tends to disappear. The expansion effects have considerably decreased as the liquid has filled the whole system. Nevertheless, a steady cavitation pocket remains attached to the nozzle throat as we can see in the last views.

5.2.4. Detonation fronts

The aim of this test is to show the capability of the method to propagate others multi-dimensional permeable fronts such as detonation waves (supersonic fronts). The reactive Riemann solver associated to detonation fronts built in Appendix A is used with the same preceding method (RDEM).

The initial situation of the simulation is represented in Fig. 23.

This situation corresponds to the impact of a copper projectile over a copper tank containing an ideal condensed explosive whose EOS parameters are given previously in the one-dimensional detonation test case. Thus, material interfaces are present as well as a permeable front (detonation wave). In this simulation, four fluids are needed: explosive, gaseous products, copper and surrounding gas. Mass transfer is only considered between the explosive and its associated products. The 'Stiffened Gas' EOS parameters of the copper with density $\rho = 8900$ kg/m^3 are $\gamma = 4.22$ and $P_\infty = 324 \times 10^8$ Pa. Those of the gas, with density $\rho = 1$ kg/m^3, are $\gamma = 1.4$ and $P_\infty = 0$ Pa. The medium is initially at atmospheric pressure and at rest except the projectile whose velocity is 2000 m/s.

The numerical results (400×400 computational cells) are given in Fig. 24 and show the temporal evolution of the detonation front propagating into the explosive. The results are represented at times $t = 10$ μs, $t = 36$ μs, $t = 51$ μs, $t = 69$ μs, $t = 88$ μs and $t = 100$ μs.

At the first instants, we clearly see that the front is not planar. Indeed, the pressure levels are higher at the corners of the tank. This leads locally to a super-detonation. The situation inverts at further instants. Expansion effects appear near the envelope resulting in a change of the front curvature. This phenomenon is experimentally observed.

6. Conclusion

A new approach for the numerical resolution of permeable fronts dynamics has been developed. It has been illustrated on several two-dimensional examples involving interfaces, supersonic or subsonic permeable fronts. The studied applications are related to evaporation and detonation waves, but we believe that the same approach can be used to propagate flame fronts, ablation fronts such as those encountered in inertial confinement fusion (ICF) [24], and others.

For each specific situation care has to be taken with the kinetic relation that allows the closure of the reactive Riemann problem. Regarding general evaporation and ablation fronts, this topic is one of the perspectives of the present work.

In the present work, the fluid thermodynamics has been restricted to the 'Stiffened Gas' EOS because it was sufficiently accurate for the applications. When dealing with other detonation applications, more sophisticated EOS may be necessary [8]. The building of the reactive Riemann solver in such context is also possible.

Acknowledgments

This work was partially supported by RENAULT Guyancourt. The authors are grateful to Martin Schaffar (ISL) and also Lazhar Houas, Georges Jourdan and Guillaume Layes (IUSTI) for providing experimental data. They address special thanks to Ashwin Chinnayya and Eric Daniel of the POLYTECH/INRIA SMASH group for their daily support and help all along this study.

Appendix A. The reactive Riemann problem with detonation waves

In this appendix, we describe the building of the reactive Riemann problem solution in the presence of detonation waves. As for evaporation fronts, this reactive Riemann problem contains a transformation

wave controlling the rate at which equilibrium is reached. This additional wave results in the production of detonation products at thermodynamic equilibrium. Such reactive Riemann problem is also well described in [9,11,18]. Its resolution has been done in [9] for ideal gases. We extend the method for the 'Stiffened Gas' EOS hereafter.

Like evaporation fronts, the detonation wave obeys the Rankine–Hugoniot relations with different 'Stiffened Gas' EOS parameters on both sides of the front:

$$\begin{cases} u = u_0 \pm sg(P-P_0)\sqrt{\frac{2(P-P_0)(P-P_v)}{\rho_0((\gamma+1)(P+P_\infty)+(\gamma-1)(P_0+P_\infty))}}, \\ m^2 = \frac{\rho_0}{2}[(\gamma+1)(P+P_\infty)+(\gamma-1)(P_0+P_\infty)]\frac{P-P_0}{P-P_v}, \\ \rho = \rho_0 \frac{\frac{\gamma+1}{\gamma-1}(P+P_\infty)+P_0+P_\infty}{\frac{\gamma_0+1}{\gamma_0-1}(P_0+P_{\infty 0})+P+P_{\infty 0}-2\rho_0\Delta q} \end{cases} \tag{A.1}$$

with ± for a right(left)-facing front, respectively. The pressure P_v, given by relation (23), corresponds to a constant volume explosion ($\rho = \rho_0$). The state with subscript 0 is the initial state of the explosive in which the detonation front propagates.

Let us examine the various waves patterns to take into account for the reactive Riemann problem.

A detonation front is always compressive ($P > P_0$) and supersonic with respect to the initial state of the explosive ($|D - u_0| > c_0$, where D is the front velocity). Consequently, no wave is preceding the front.

The CJ detonation condition $|D - u| = c$ expresses the front stability because the backward waves cannot reach the front. The Rankine–Hugoniot system is thus closed by the CJ relation and it is useless to give any additional value behind the front.

The front velocity can be higher than the CJ one with superdetonations (upper part of the CJ detonation point in Fig. 8). It happens when the pressure behind the front is higher than the CJ one. Then, it is necessary to use the value of the pressure to close the Rankine–Hugoniot system. Indeed, in such situations, backward waves reach the front that is subsonic with respect to the detonation products ($|D - u| < c$). Nevertheless, this situation occurs only in unsteady conditions when a piston sustains the strong detonation. As the front velocity is higher than the piston one the detonation wave cannot be supported by the piston over a long time period. It recovers quickly its stable state and propagates at CJ velocity.

The curve below the CJ detonation point in Fig. 8 corresponds to weak detonations. In this case, the front is supersonic with respect to the detonation products ($|D - u| > c$). Consequently, the state behind the front cannot influence the wave that remains sustained by the CJ detonation condition. Rarefaction waves (Taylor expansion wave) appear immediately behind the front connecting the CJ state to the products state. This waves pattern, named CJ detonation, is observed in most cases when the products pressure is lower than the CJ one.

As for evaporation fronts, two waves patterns exist with detonations :

- a superdetonation front when the products pressure is higher than the CJ one (single wave),
- a CJ detonation front followed by a Taylor expansion wave when products pressure is lower than the CJ one (composite wave).

Like evaporation phenomena, the resolution of the reactive Riemann problem depends on a 'reactivity factor' of the explosive, here an ignition pressure P_{ig}.

First, the inert Riemann problem is solved. On both sides of the contact discontinuity u^*, we compare, if the fluid corresponds to an explosive, the solution P^* with its characteristic ignition pressure P_{ig}.

If $P^* < P_{ig}$, the explosive remains inert and the whole solution is obtained with the inert Riemann solver. If $P^* > P_{ig}$, the explosive reacts and the reactive Riemann problem has to be solved.

Similarly to the evaporation problem, this one is solved by iterating over the pressure P^* at the contact discontinuity. At each iteration, the pressure P^* determines the waves pattern (Fig. 25) connecting the left and right states to this pressure.

Let us recall that, in the inert case, two instances are possible:

- if $P^* \geqslant P_0$, Rankine–Hugoniot relations (13) are used,
- if $P^* \leqslant P_0$, isentropic relations (11) are used.

When the fluid is reactive, two other instances are possible:

- if $P^* \geqslant P_{CJ}$, the front is a superdetonation and relations (A.1) are used,
- if $P^* \leqslant P_{CJ}$, the front is a CJ detonation and isentropic relations (11) are used to connect the pressure P^* to the CJ state determined by relation (36).

All these relations write in a common form:

$$u^* = u_0 \pm \phi_0(P^*), \tag{A.2}$$

with

$$\phi_0(P^*) = \begin{cases} \dfrac{P^* - P_0}{\rho_0 c_0 \sqrt{\frac{\gamma_0+1}{2\gamma_0}\left(\frac{P^*+P_{\infty 0}}{P_0+P_{\infty 0}}\right)+\frac{\gamma_0-1}{2\gamma_0}}} & \text{if } P^* > P_0 \text{ (inert)}, \\ \dfrac{2c_0}{\gamma_0-1}\left(\left(\dfrac{P^*+P_{\infty 0}}{P_0+P_{\infty 0}}\right)^{(\gamma_0-1)/2\gamma_0} - 1\right) & \text{if } P^* \leqslant P_0 \text{ (inert)}, \\ \sqrt{\dfrac{2(P^*-P_0)(P^*-P_v)}{\rho_0((\gamma+1)(P^*+P_\infty)+(\gamma-1)(P_0+P_\infty))}} & \text{if } P^* > P_{CJ} \text{ (reactive)}, \\ u_{CJ} - u_0 + \dfrac{2c_{CJ}}{\gamma-1}\left(\left(\dfrac{P^*+P_\infty}{P_{CJ}+P_\infty}\right)^{(\gamma-1)/2\gamma} - 1\right) & \text{if } P^* \leqslant P_{CJ} \text{ (reactive)}. \end{cases} \tag{A.3}$$

Now substituting subscript 0 in (A.2) and (A.3) by subscripts L and R corresponding to the left and right states, respectively, we get:

$$u^* = u_L - \phi_L(P^*), \tag{A.4}$$

$$u^* = u_R + \phi_R(P^*). \tag{A.5}$$

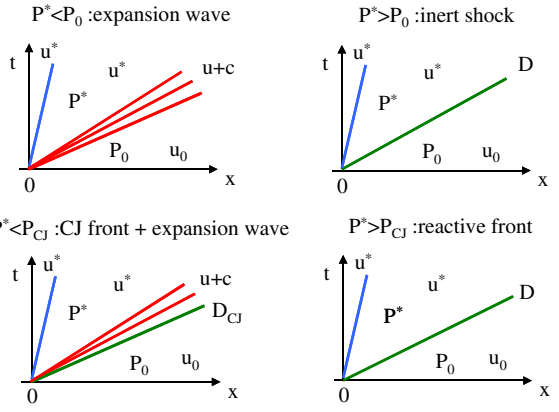

Fig. 25. Waves patterns in the reactive Riemann problem associated to detonation fronts.

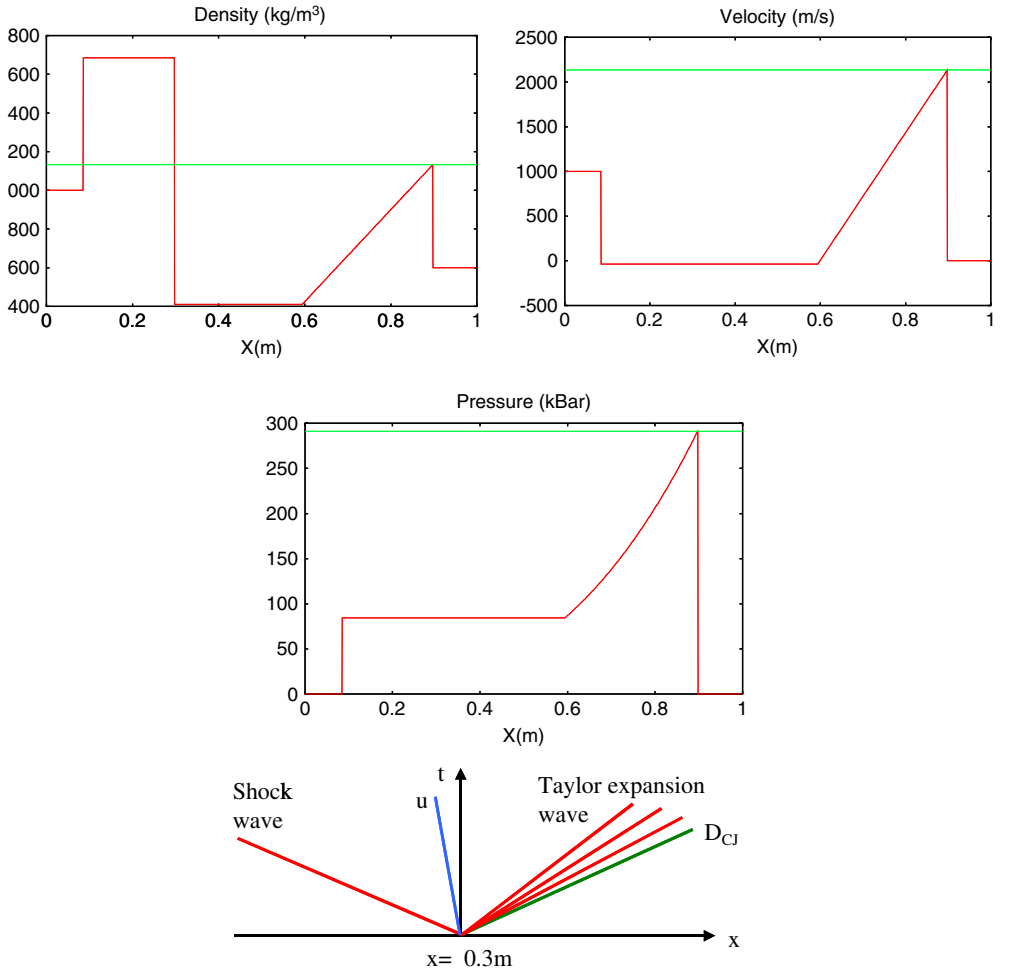

Fig. 26. Exact solution of a reactive Riemann problem with a CJ detonation front. The horizontal lines represent the theoretical values of the CJ detonation state.

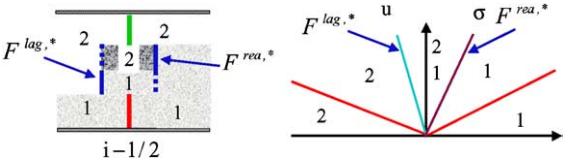

Fig. 27. Lagrangian and reactive fluxes in the Riemann problem (2−1) for a partial evaporation front.

Table 7
Notations associated with the resolution of Riemann problems

Notations	Significations
(*TR*)	Reactive Riemann problem with a total evaporation front
(*PR*)	Reactive Riemann problem with a partial evaporation front
(*I*)	Inert Riemann problem

Combining Eqs. (A.4) and (A.5) a scalar equation is obtained:

$$F(P^*) = u_R - u_L + \phi_R(P^*) + \phi_L(P^*) = 0. \tag{A.6}$$

The solution P^* is determined by an iterative algorithm (Newton–Raphson for example). Once P^* is obtained, it is easy to determine the whole solution from the corresponding waves patterns relations.

Table 8
The different configurations for Eulerian fluxes at cell boundary $i - 1/2$ for fluid $k = 1$ in the presence of partial or total evaporation fronts

Contact	Type	Eulerian flux	Phase function χ_1^*
1–1	(I)	F_{11}^*	$\chi_{1,11}^* = 1$
	$(TR)_l$	F_{11}^*	$\chi_{1,11}^* = \begin{cases} 0 & \text{if } \sigma_{11,l}^* < 0 < u_{11}^* \\ 1 & \text{otherwise} \end{cases}$
	$(TR)_r$	F_{11}^*	$\chi_{1,11}^* = \begin{cases} 0 & \text{if } u_{11}^* < 0 < \sigma_{11,r}^* \\ 1 & \text{otherwise} \end{cases}$
	$(TR)_l$ $(TR)_r$	F_{11}^*	$\chi_{1,11}^* = \begin{cases} 0 & \text{if } \sigma_{11,l}^* < 0 < \sigma_{11,r}^* \\ 1 & \text{otherwise} \end{cases}$
	$(PR)_l$ $(TR)_r$	$\begin{cases} (\alpha_1^* F_1^*)_{11,l} & \text{if } \sigma_{11,l}^* < 0 < u_{11}^* \\ F_{11}^* & \text{otherwise} \end{cases}$	$\chi_{1,11}^* = \begin{cases} 0 & \text{if } u_{11}^* < 0 < \sigma_{11,r}^* \\ 1 & \text{otherwise} \end{cases}$
	$(TR)_l$ $(PR)_r$	$\begin{cases} (\alpha_1^* F_1^*)_{11,r} & \text{if } u_{11}^* < 0 < \sigma_{11,r}^* \\ F_{11}^* & \text{otherwise} \end{cases}$	$\chi_{1,11}^* = \begin{cases} 0 & \text{if } \sigma_{11,l}^* < 0 < u_{11}^* \\ 1 & \text{otherwise} \end{cases}$
	$(PR)_l$	$\begin{cases} (\alpha_1^* F_1^*)_{11,l} & \text{if } \sigma_{11,l}^* < 0 < u_{11}^* \\ F_{11}^* & \text{otherwise} \end{cases}$	$\chi_{1,11}^* = 1$
	$(PR)_r$	$\begin{cases} (\alpha_1^* F_1^*)_{11,r} & \text{if } u_{11}^* < 0 < \sigma_{11,r}^* \\ F_{11}^* & \text{otherwise} \end{cases}$	$\chi_{1,11}^* = 1$
	$(PR)_l$ $(PR)_r$	$\begin{cases} (\alpha_1^* F_1^*)_{11,r} & \text{if } u_{11}^* < 0 < \sigma_{11,r}^* \\ (\alpha_1^* F_1^*)_{11,l} & \text{if } \sigma_{11,l}^* < 0 < u_{11}^* \\ F_{11}^* & \text{otherwise} \end{cases}$	$\chi_{1,11}^* = 1$
1–2	(I)	F_{12}^*	$\chi_{1,12}^* = \begin{cases} 1 & \text{if } u_{12}^* > 0 \\ 0 & \text{otherwise} \end{cases}$
	(TR)	F_{12}^*	$\chi_{1,12}^* = \begin{cases} 1 & \text{if } \sigma_{12}^* > 0 \\ 0 & \text{otherwise} \end{cases}$
	(PR)	$\begin{cases} (\alpha_1^* F_1^*)_{12} & \text{if } \sigma_{12}^* < 0 < u_{12}^* \\ F_{12}^* & \text{otherwise} \end{cases}$	$\chi_{1,12}^* = \begin{cases} 1 & \text{if } u_{12}^* > 0 \\ 0 & \text{otherwise} \end{cases}$
	(I)	F_{21}^*	$\chi_{1,21}^* = \begin{cases} 1 & \text{if } u_{21}^* < 0 \\ 0 & \text{otherwise} \end{cases}$
2–1	(TR)	F_{21}^*	$\chi_{1,21}^* = \begin{cases} 1 & \text{if } \sigma_{21}^* < 0 \\ 0 & \text{otherwise} \end{cases}$
	(PR)	$\begin{cases} (\alpha_1^* F_1^*)_{21} & \text{if } u_{21}^* < 0 < \sigma_{21}^* \\ F_{21}^* & \text{otherwise} \end{cases}$	$\chi_{1,21}^* = \begin{cases} 1 & \text{if } u_{21}^* < 0 \\ 0 & \text{otherwise} \end{cases}$
2–2	(I)	F_{22}^*	$\chi_{1,22}^* = 0$

Table 9
The different configurations for Lagrangian fluxes at cell boundary $i-1/2$ for fluid $k=1$ in the presence of partial or total evaporation fronts

Contact	Type	Lagrangian flux	Jump $[\chi_1^x]^*$
1–1	(I)	$F_{11}^{\mathrm{lag},*}$	$[\chi_1^x]_{11}^* = 0$
	$(TR)_\mathrm{l}$	$F_{11}^{\mathrm{lag},*}$	$[\chi_1^x]_{11}^* = \begin{cases} 1 & \text{if } u_{11}^* > 0 \\ 0 & \text{otherwise} \end{cases}$
	$(TR)_\mathrm{r}$	$F_{11}^{\mathrm{lag},*}$	$[\chi_1^x]_{11}^* = \begin{cases} -1 & \text{if } u_{11}^* > 0 \\ 0 & \text{otherwise} \end{cases}$
	$(TR)_\mathrm{l}$ $(TR)_\mathrm{r}$	$F_{11}^{\mathrm{lag},*}$	$[\chi_1^x]_{11}^* = 0$
	$(PR)_\mathrm{l}$ $(TR)_\mathrm{r}$	$(\alpha_{1,\mathrm{l}}^* F^{\mathrm{lag},*})_{11}$	$[\chi_1^x]_{11}^* = \begin{cases} -1 & \text{if } u_{11}^* > 0 \\ 0 & \text{otherwise} \end{cases}$
	$(TR)_\mathrm{l}$ $(PR)_\mathrm{r}$	$(\alpha_{1,\mathrm{r}}^* F^{\mathrm{lag},*})_{11}$	$[\chi_1^x]_{11}^* = \begin{cases} 1 & \text{if } u_{11}^* > 0 \\ 0 & \text{otherwise} \end{cases}$
	$(PR)_\mathrm{l}$	$\left((1-\alpha_{1,\mathrm{l}}^*)F^{\mathrm{lag},*}\right)_{11}$	$[\chi_1^x]_{11}^* = \begin{cases} 1 & \text{if } u_{11}^* > 0 \\ 0 & \text{otherwise} \end{cases}$
	$(PR)_\mathrm{r}$	$\left((1-\alpha_{1,\mathrm{r}}^*)F^{\mathrm{lag},*}\right)_{11}$	$[\chi_1^x]_{11}^* = \begin{cases} -1 & \text{if } u_{11}^* > 0 \\ 0 & \text{otherwise} \end{cases}$
	$(PR)_\mathrm{l}$ $(PR)_\mathrm{r}$	$\left(\lvert\alpha_{1,\mathrm{r}}^* - \alpha_{1,\mathrm{l}}^*\rvert F^{\mathrm{lag},*}\right)_{11}$	$[\chi_1^x]_{11}^* = \begin{cases} \mathrm{sgn}\left(\alpha_{1,\mathrm{r}}^* - \alpha_{1,\mathrm{l}}^*\right)_{11} & \text{if } u_{11}^* > 0 \\ 0 & \text{otherwise} \end{cases}$
1–2	(I)	$F_{12}^{\mathrm{lag},*}$	$[\chi_1^x]_{12}^* = \begin{cases} -1 & \text{if } u_{12}^* > 0 \\ 0 & \text{otherwise} \end{cases}$
	(TR)	$F_{12}^{\mathrm{lag},*}$	$[\chi_1^x]_{12}^* = 0$
	(PR)	$(\alpha_1^* F^{\mathrm{lag},*})_{12}$	$[\chi_1^x]_{12}^* = \begin{cases} -1 & \text{if } u_{12}^* > 0 \\ 0 & \text{otherwise} \end{cases}$
2–1	(I)	$F_{21}^{\mathrm{lag},*}$	$[\chi_1^x]_{21}^* = \begin{cases} 1 & \text{if } u_{21}^* > 0 \\ 0 & \text{otherwise} \end{cases}$
	(TR)	$F_{21}^{\mathrm{lag},*}$	$[\chi_1^x]_{21}^* = 0$
	(PR)	$(\alpha_1^* F^{\mathrm{lag},*})_{21}$	$[\chi_1^x]_{21}^* = \begin{cases} 1 & \text{if } u_{21}^* > 0 \\ 0 & \text{otherwise} \end{cases}$
2–2	(I)	$F_{22}^{\mathrm{lag},*}$	$[\chi_1^x]_{22}^* = 0$

An example of solution is provided hereafter.

A fluid at velocity $u = 1000$ m/s, with density $\rho = 2000$ kg/m^3 impacts an explosive at rest whose density is $\rho = 1600$ kg/m^3. The EOS parameters of the impactor are $\gamma = 4$ and $P_\infty = 3\,10^9$ Pa. The parameters of the explosive are $\gamma = 3$, $P_\infty = 0$ Pa and $q = 4.56 \times 10^6$ J/kg. Those of the detonation product are the same but with $q = 0$ J/kg. The initial impact is located at $x = 0.3$ m in a 1 m length tube at atmospheric pressure. The exact solution is represented at time $t = 70$ μs in Fig. 26.

Table 10
The different configurations for reactive fluxes at cell boundary $i-1/2$ for fluid $k = 1$ in the presence of partial or total evaporation fronts

Contact	Type	Reactive flux	Jump $[\chi_1^x]^*$
1–1	$(TR)_l$	$F_{11,l}^{rea,*}$	$[\chi_1^x]_{11}^* = \begin{cases} -1 & \text{if } \sigma_{11,l}^* > 0 \\ 0 & \text{otherwise} \end{cases}$
	$(TR)_r$	$F_{11,r}^{rea,*}$	$[\chi_1^x]_{11}^* = \begin{cases} 1 & \text{if } \sigma_{11,r}^* > 0 \\ 0 & \text{otherwise} \end{cases}$
	$(PR)_l$	$\left((1-\alpha_1^*)F^{rea,*}\right)_{11,l}$	$[\chi_1^x]_{11}^* = \begin{cases} -1 & \text{if } \sigma_{11,l}^* > 0 \\ 0 & \text{otherwise} \end{cases}$
	$(PR)_r$	$\left((1-\alpha_1^*)F^{rea,*}\right)_{11,r}$	$[\chi_1^x]_{11}^* = \begin{cases} 1 & \text{if } \sigma_{11,r}^* > 0 \\ 0 & \text{otherwise} \end{cases}$
1–2	(TR)	$F_{12}^{rea,*}$	$[\chi_1^x]_{12}^* = \begin{cases} -1 & \text{if } \sigma_{12}^* > 0 \\ 0 & \text{otherwise} \end{cases}$
	(PR)	$\left((1-\alpha_1^*)F^{rea,*}\right)_{12}$	$[\chi_1^x]_{12}^* = \begin{cases} -1 & \text{if } \sigma_{12}^* > 0 \\ 0 & \text{otherwise} \end{cases}$
2–1	(TR)	$F_{21}^{rea,*}$	$[\chi_1^x]_{21}^* = \begin{cases} 1 & \text{if } \sigma_{21}^* > 0 \\ 0 & \text{otherwise} \end{cases}$
	(PR)	$\left((1-\alpha_1^*)F^{rea,*}\right)_{21}$	$[\chi_1^x]_{21}^* = \begin{cases} 1 & \text{if } \sigma_{21}^* > 0 \\ 0 & \text{otherwise} \end{cases}$

The solution consists in a right-facing CJ detonation front propagating into the explosive followed by a Taylor expansion wave and a left-facing shock wave propagating into the impactor. The different values of the CJ detonation state with respect to the explosive initial state are $\rho_{CJ} = 2133$ kg/m^3, $u_{CJ} = 2135$ m/s and $P_{CJ} = 291.8 \times 10^8$ Pa, as shown by the horizontal lines in Fig. 26.

Appendix B. Implementation of partial evaporation fronts in the reactive discrete equations method (RDEM)

As we have seen in Section 4, the coupling of the reactive Riemann problem with the discrete equations method leads to additional terms associated to evaporation fronts : the reactive fluxes. In Section 4, we have considered total evaporation fronts where only vapor is produced behind the front. In this appendix we extend the method to partial evaporation fronts where a mixture of liquid and vapor at thermodynamic equilibrium is present behind the front, as shown in Fig. 27.

In this case, we must take into account the fact that a part of the liquid does not transform into vapor across the evaporation front. Consequently, jumps of the phase functions are zero inside this volume fraction. Moreover, at the contact discontinuity, two types of contacts between fluids are also available (vapor–liquid and vapor–vapor).

For the sake of clarity, we adopt some notations indicating the presence of total or partial evaporation fronts in the reactive Riemann problem solution as represented in Table 7.

When the evaporation is partial across the front, both phases (liquid and vapor) may coexist at $x/t = 0$. The Eulerian fluxes $F_k^* = (\rho_k u, \rho_k u^2 + P, \rho_k uv, (\rho_k E_k + P)u)^{T,*}$ of the two phases are available within the mixture at thermodynamic equilibrium. Their respective volume fraction α_k^* within this mixture are also given by the resolution of the reactive Riemann problem, more precisely by the relation (30). Thus, if the sampling corresponds to the mixture zone, the retained Eulerian flux is $\alpha_k^* F_k^*$ for each phase k. Then,

the different configurations for the Eulerian fluxes calculations in Table 4 are replaced by those of Table 8, where we have removed deliberately the contact surfaces that remain unchanged.

Regarding Lagrangian and reactive fluxes, the phase functions have jumps not only at contact discontinuities but also across evaporation fronts, as represented in Fig. 27. These jumps depend directly on the volumes occupied by the two phases within the mixture behind the partial evaporation fronts.

Note also that when partial evaporation occurs (type (PR)), the resulting Lagrangian flux is the product $\alpha F^{lag,*}$ where α is the volume fraction through which the jump is non zero. Obviously α depends on the volume fraction α_k^* of each phase given by the reactive Riemann solver. For example, in the particular Riemann problem (1−1) where two partial evaporation fronts ($\sigma_{11,l}^*$ and $\sigma_{11,r}^*$) may coexist, the Lagrangian fluxes and jumps are calculated according to the volumes occupied by the phases on both sides of the contact discontinuity u_{11}^*. The different configurations for the calculations of the Lagrangian fluxes are summarized in Table 9.

The same considerations are used for the reactive fluxes calculations that are summarized in Table 10.

The discrete equations of the system (52) remains unchanged but the different terms have to be calculated with the ingredients provided in these tables.

References

[1] R. Abeyaratne, J. Knowles, Kinetic relations and the propagation of phase boundaries in solids, Arch. Rat. Mech. Anal. 114 (1991) 119–154.

[2] R. Abgrall, R. Saurel, Discrete equations for physical and numerical compressible multiphase mixtures, J. Comp. Phys. 186 (2003) 361–396.

[3] C. Arcoumanis, M. Gavaises, H. Flora, H. Roth, Visualisation of cavitation in diesel engine injectors, Mec. Ind. 2 (2001) 375–381.

[4] C. Badock, R. Wirth, A. Fath, A. Leipertz, Investigation of cavitation in real size diesel injection nozzles, Int. J. Heat Fluid Flow 20 (1999) 538–544.

[5] M.R. Baer, J.W. Nunziato, A two-phase mixture theory for the deflagration-to-detonation transition (DDT) in reactive granular materials, Int. J. Multiphase Flows 12 (1986) 861–889.

[6] J.B. Bdzil, D.S. Stewart, Modelling two-dimensional detonation with detonation shock dynamics, Phys. Fluids A 1 (1989) 1261–1267.

[7] L. Brun, Un nouveau modèle macroscopique de la détonation non soutenue dans les explosifs condensés. 3rd International Symposium on High Dynamic Pressures – La Grande Motte, (1989) 103–107.

[8] A. Chinnayya, E. Daniel, R. Saurel, Modelling detonation waves in heterogeneous energetic materials, J. Comp. Phys. 196 (2004) 490–538.

[9] A.J. Chorin, Random choice methods with applications to reacting gas flow, J. Comp. Phys. 25 (1977) 253–272.

[10] P. Clavin, P. Garcia, The influence of the temperature dependence of diffusivities on the dynamics flame Fronts, J. Mécanique Théorique et Appliquée 2 (1983) 245–263.

[11] R. Courant, K.O. Friedrichs, Supersonic flow and shock wavesApplied Mathematical Sciences, vol. 21, Springer-Verlag, 1948.

[12] D.A. Drew, S.L. Passman, Theory of multicomponent fluids, Springer, 1998.

[13] W. Fickett, W.C. Davis, Detonation, University of California Press, 1979.

[14] C. Fouillet, Généralisation à des mélanges binaires de la méthode du second gradient et application à la simulation numérique directe de l'ébullition nucléée. Ph.D Thesis, Université Paris VI, 2003.

[15] D.L. Frost, J.H.S. Lee, G. Ciccarelli, The use of Hugoniot analysis for the propagation of vapor explosion waves, Shock Waves 1 (1991) 99–110.

[16] S. Gavrilyuk, R. Saurel, Mathematical and numerical modelling of two-phase compressible flows with micro-inertia, J. Comp. Phys. 175 (1) (2002) 326–360.

[17] J. Glimm, Comm. Pure Appl. Math. 18 (1965) 697.

[18] E. Godlewski, P.-A. Raviart, Numerical approximation of hyperbolic systems of conservation lawsApplied Mathematical Sciences, vol. 118, Springer-Verlag, 1996.

[19] F. Harlow, A. Amsden, Fluid dynamics. monograph LA-4700. Los Alamos National Laboratory, NM, 1971.

[20] D. Jamet, O. Lebaigue, N. Coutris, J.M. Delhaye, The second gradient method for the direct numerical simulation of liquid–vapor flows with phase change, J. Comp. Phys. 169 (2001) 624–651.

[21] Th. Kurschat, H. Chaves, G.E.A. Meier, Complete adiabatic evaporation of highly superheated liquid jets, J. Fluid Mech. 236 (1992) 43–59.
[22] P.G. LeFloch, C. Rohde, High-order schemes, entropy inequalities and nonclassical shocks, SIAM J. Numer. Anal. 37 (6) (2000) 2023–2060.
[23] O. LeMetayer, J. Massoni, R. Saurel, Élaboration des Lois d'État d'un Liquide et de sa Vapeur pour les Modèles d'Écoulements Diphasiques, Int. J. Thermal Sci. 43 (2003) 265–276.
[24] L. Masse, Etude Linéaire de l'Instabilité du Front d'Ablation en Fusion par Confinement Inertiel. Ph.D Thesis, Université Aix-Marseille I, 2001.
[25] R. Menikoff, B.J. Plohr, The Riemann problem for fluid flow of real materials, Rev. Mod. Phys. 61 (1989) 75–130.
[26] R. Oldenbourg, Properties of Water and Steam in SI-Units, Springer-Verlag, Berlin Heidelberg, New York, 1989.
[27] R.C. Reid, J.M. Prausnitz, B.E. Poling, The Properties of Gases and Liquids, fourth ed., Mc Graw-Hill, 1987.
[28] P. Reinke, G. Yadigaroglu, Explosive vaporization of superheated liquids by boiling fronts, Int. J. Multiphase Flows 27 (2001) 1487–1516.
[29] R. Saurel, S. Gavrilyuk, F. Renaud, A multiphase model with internal degrees of freedom: application to shock–bubble interaction, J. Fluid. Mech. 495 (2003) 283–321.
[30] R. Saurel, O. LeMetayer, A multiphase model for compressible flows with interfaces, shocks, detonation waves and cavitation, J. Fluid. Mech. 431 (2001) 239–271.
[31] M. Schaffar, C. Rey, G. Boeglen, Résultats des Essais de Faisabilité de Projectiles Supercavitants tirés Horizontalement dans l'Eau. Rapport de Recherche ISL, R106/2003, Institut Franco-Allemand de Recherches de Saint-Louis, 2003.
[32] J.R. Simões-Moreira, J.E. Shepherd, Evaporation waves in superheated dodecane, J. Fluid Mech. 382 (1999) 63–86.
[33] J.R. Simões-Moreira, Adiabatic Evaporation Waves. Ph.D Thesis, Rensselaer Polytechnic Institute, Troy, New York, 1994.
[34] M. Slemrod, Admissibility criteria for propagating phase boundaries in a van der Waals fluid, Arch. Rat. Mech. Anal. 81 (1983) 301–315.
[35] Z.-H. Teng, A.J. Chorin, T.-P. Liu, Riemann problems for reacting gas, with applications to transition, SIAM J. Appl. Math. 42 (5) (1982) 964–981.
[36] P.A. Thompson, H. Chaves, G.E.A. Meier, Y.-G. Kim, H.-D. Speckmann, Wave splitting in a fluid of large heat capacity, J. Fluid Mech. 185 (1987) 385–414.
[37] E.F. Toro, Riemann Solvers and Numerical Methods for Fluid Dynamics, Springer, 1997.
[38] L. Truskinovsky, Kinks versus shocks, in: Shock Induced Transitions and Phase Structures in General MediaIMA, 52, Springer-Verlag, Berlin, 1991.
[39] A.B. Wood, A Textbook of Sound, The Macmillan Company, New York, 1930, 327.
[40] W.W. Wood, J.G. Kirkwood, Diameter effect in condensed explosives: the relation between velocity and radius of curvature in the detonation wave, J. Chem. Phys. 22 (1954) 1920–1928.